



The 12th June 2017 $M_w = 6.3$ Lesvos earthquake from detailed seismological observations



P. Papadimitriou^{a,*}, I. Kassaras^a, G. Kaviris^a, G.-A. Tselentis^{a,c}, N. Voulgaris^a, E. Lekkas^b, G. Chouliaras^c, C. Evangelidis^c, K. Pavlou^a, V. Kapetanidis^a, A. Karakonstantis^a, D. Kazantzidou-Firtinidou^a, I. Fountoulakis^a, C. Millas^a, I. Spingos^a, T. Aspiotis^a, A. Moumoulidou^a, E. Skourtsos^b, V. Antoniou^b, E. Andreadakis^b, S. Mavroulis^b, M. Kleanthi^d

^a Department of Geophysics-Geothermics, Faculty of Geology and Geoenvironment, National and Kapodistrian University of Athens, Panepistimiopolis, 157 84, Zografou, Greece

^b Department of Dynamic, Tectonic and Applied Geology, Faculty of Geology and Geoenvironment, National and Kapodistrian University of Athens, Panepistimiopolis, 157 84, Zografou, Greece

^c Geodynamic Institute, National Observatory of Athens, Lofos Nymfon, Thission, 11810, Athens, Greece

^d ERO-DAEFK, Konari 43, 114 71, Athens, Greece

ARTICLE INFO

Keywords:

Seismotectonics
Aftershock relocation
Focal mechanism
Stress inversion
Coulomb stress
North Aegean

ABSTRACT

A major earthquake ($M_w = 6.3$) occurred on the 12th of June 2017 (12:28 GMT) offshore, south of the SE coast of Lesvos Island, at a depth of 136 km, in an area characterized by normal faulting with an important strike-slip component in certain cases. Over 900 events of the sequence between 12 and 30 June 2017 were manually analyzed and located, employing an optimized local velocity model. Double-difference relocation revealed seven spatially separated groups of events, forming two linear branches, roughly aligned N130°E, compatible with the strike of known mapped faults along the southern coast of Lesvos Island. Spatiotemporal analysis indicated gradual migration of seismicity towards NW and SE from the margins of the main rupture, while a strong secondary sequence at a separate fault patch SE of the mainshock, oriented NW-SE, was triggered by the largest aftershock ($M_w = 5.2$) that occurred on 17 June. The focal mechanisms of the mainshock ($\phi = 122^\circ$, $\delta = 40^\circ$ and $\lambda = -83^\circ$) and of the major aftershocks were determined using regional moment tensor inversion. In most cases normal faulting was revealed with the fault plane oriented in a NW-SE direction, dipping SW, with the exception of the largest aftershock that was characterized by strike-slip faulting. Stress inversion revealed a complex stress field south of Lesvos, related both to normal, in an approximate E-W direction, and strike-slip faulting. All aftershocks outside the main rupture, where gradual seismicity migration was observed, are located within the positive lobes of static stress transfer determined by applying the Coulomb criterion for the mainshock. Stress loading on optimal faults under a strike-slip regime explains the occurrence of the largest aftershock and the seismicity that was triggered at the eastern patch of the rupture zone.

1. Introduction

On 12 June 2017, a shallow crustal strong earthquake with magnitude 6.3 occurred offshore, south of Lesvos (12:28 GMT), 35.8 km SSW of the capital of Lesvos Island, Mytilene (Fig. 1), causing one fatality and severe structural damage in the SE part of the island. The event was strongly felt in the north Aegean islands and the neighboring

Turkish coasts, while it was also felt in the Greek mainland. The severity of ground motion was not instrumentally recorded in the epicentral area, since the closest accelerograph in Greece was at a distance of ~36 km. The hypocenter of the mainshock was automatically determined by the Seismological Laboratory of the National and Kapodistrian University of Athens (SL-NKUA) and the solution was promptly available online for the public. This study presents the effects of the

* Corresponding author.

E-mail addresses: ppapadim@geol.uoa.gr (P. Papadimitriou), kassaras@geol.uoa.gr (I. Kassaras), gkaviris@geol.uoa.gr (G. Kaviris), gtselentis@geol.uoa.gr (G.-A. Tselentis), voulgaris@geol.uoa.gr (N. Voulgaris), elekkas@geol.uoa.gr (E. Lekkas), g.choul@noa.gr (G. Chouliaras), cevan@noa.gr (C. Evangelidis), kpavlou@geol.uoa.gr (K. Pavlou), vkapetan@geol.uoa.gr (V. Kapetanidis), akarakon@geol.uoa.gr (A. Karakonstantis), dkazantzidou@geol.uoa.gr (D. Kazantzidou-Firtinidou), fountoul@geol.uoa.gr (I. Fountoulakis), cmillas@geol.uoa.gr (C. Millas), ispingos@geol.uoa.gr (I. Spingos), tedaspiotis@geol.uoa.gr (T. Aspiotis), amoumoul@geol.uoa.gr (A. Moumoulidou), eskourt@geol.uoa.gr (E. Skourtsos), vantoniu@geol.uoa.gr (V. Antoniou), eandreadk@geol.uoa.gr (E. Andreadakis), smavroulis@geol.uoa.gr (S. Mavroulis), gdaefk@ggde.gr (M. Kleanthi).

<https://doi.org/10.1016/j.jog.2018.01.009>

Received 28 July 2017; Received in revised form 5 December 2017; Accepted 17 January 2018

Available online 31 January 2018

0264-3707/© 2018 Elsevier Ltd. All rights reserved.

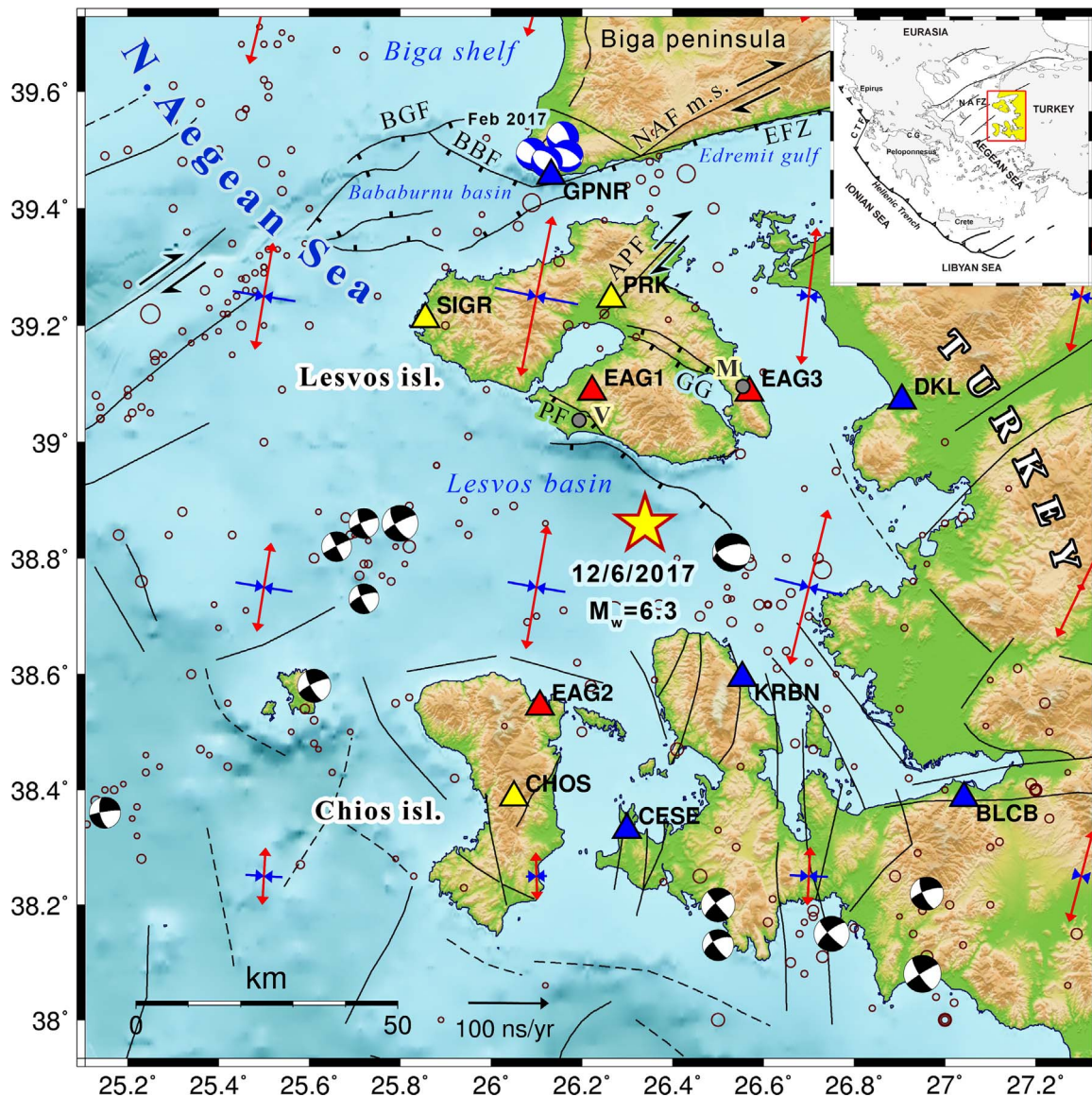


Fig. 1. Seismotectonic map of the broader Lesvos area. Solid triangles are recording stations used in this study from HUSN (yellow), the GI-NOA temporary network (red) and KOERI (blue). Empty circles are instrumental earthquakes with $M \geq 4$ (Makropoulos et al., 2012). Black beachballs are CMT solutions (Ekström et al., 2012) of earthquakes with $M \geq 6$ and blue are solutions of earthquakes with $M > 5$ from the 2017 Biga peninsula sequence (<http://www.geophysics.geol.uoa.gr>). Faults lines are after Altinok et al. (2012), Yaltrak et al. (2012), Lekkas et al. (2017a). APF: Agia Paraskevi Fault, BBF: Bababurnu Fault, BGF: Biga Fault, EFZ: Edremit Fault Zone GG: Gulf of Gera, M: Mytilene, NAF m.s.: North Anatolian Fault middle segment, PF: Polichnitos Fault and V: Vrissa. The inset minimap shows the location of Fig. 1 within the regional system of lithospheric plates. (For interpretation of the references to colour in this figure legend, the reader is referred to the web version of this article.)

mainshock derived from instrumental and in-situ observations and investigates in detail the dynamics and evolution of the seismic sequence.

Lesvos Island is located in the north Aegean Sea, west of the coast of NW Asia Minor (Turkey) (Fig. 1). Lesvos is part of an old volcanic center in the east Aegean Sea that was active 15–19 My ago (Hecht, 1972; Pe-Piper, 1978; Katsikatos et al., 1986). The famous Sigrí Petrified Forest, one of the most beautiful monuments of geological heritage globally, was formed during that period as enormous quantities of ash and lavas covered the rich flora at the western part of Lesvos Island (e.g. Zouros et al., 2011). The geology of the island can be summarized as a basement composed of metamorphic rocks overlain by post-Alpine formations, comprising Miocene volcanic rocks and Neogene marine and lacustrine deposits (Soulakellis et al., 2006).

Geological (Pe-Piper and Piper, 1993), seismological (e.g. Papazachos et al., 1984; Kiratzi et al., 1991; Taymaz et al., 1991; Barakou et al., 2001) and geodesy data (e.g. Barka and Reilinger, 1997) indicate that the region's deformation is driven by transtensional

tectonics (Reilinger et al., 1997; Kahle et al., 1998; Yaltrak and Alpar, 2002), including E-W normal and NE-SW strike-slip faulting. Seismic reflection data suggest that basin-bounding faults, exhibiting primarily apparent normal offsets, as well as positive and negative flower structures, reflect strike-slip geometry (Maley and Johnson, 1971; Ferentinos et al., 1981; Saner, 1985; Mascle and Martin, 1990; Roussos and Lyssimachou, 1991; Çağatay et al., 1998; Saatçilar et al., 1999; Yaltrak et al., 2000). The above-mentioned complex deformation has been associated with intense seismicity (Makropoulos and Burton, 1981; Taymaz et al., 2007; Yolsal-Çevikbilen et al., 2014).

The tectonic evolution of Lesvos Island is affected by the general neotectonic evolution of the Aegean, which started in the Oligocene (15 Myr). Tectonic analysis of faults and micro-ruptures of the island (Hecht, 1974a, 1974b; Katsikatos et al., 1982) revealed three main fault systems striking $N40-60^{\circ}W$, $N30-60^{\circ}E$ and E-W, respectively (Fig. 1). The Agia Paraskevi Fault (APF) is an almost pure dextral strike-slip fault, forming a series of elongated valleys in a NNE–SSW

direction (Chatzipetros et al., 2013). APF is the only fault that has been associated with historical earthquakes in Lesvos (i.e. the 1867 event, Papazachos and Papazachou, 2003). NW-SE trending normal faults control the northern margins of the Gulf of Gera (GG) in eastern Lesvos (Chatzipetros et al., 2013) (Fig. 1). Polichnitos normal Fault (PF in Fig. 1) is an onshore marginal fault of the structurally complex Lesvos Basin, bounded by NW-SE striking normal faults characterized by numerous slumps and mass slides due to tilting of the basin margin (Mascle and Martin, 1990). From the published interpreted seismic section of Mascle and Martin (1990), it appears that Lesvos Basin is an asymmetrical graben, with the main marginal fault being the northeast one that dips SW, while antithetic faults dipping NE are found on its hangingwall. To the north, Bababurnu basin, which is located NW of Lesvos and SW of Biga Peninsula, is considered to be a transtensional basin correlated with the middle branch of the North Anatolia Fault Zone (NAFZ) (Yaltirak and Alpar, 2002). This basin is defined by NE- and SE-striking faults.

The region struck by the 12th June 2017 earthquake, has suffered several strong and destructive earthquakes since the antiquity (Papazachos and Papazachou, 2003; Makropoulos et al., 2012; Stucchi et al., 2013) (Table A1 in Appendix A). The event that presents most similarities with the 12th June 2017 earthquake is the historical one that occurred on 11 October 1845 ($M = 6.7$, $I_{EMS98} = 8.5$) (Taxeidis, 2003; Kouskouna and Sakkas, 2013). In Vrissa, 60 houses were collapsed and a woman was killed. In Plomari, 8 houses were destroyed and 40 were damaged, whereas nearby villages were also heavily affected (Papazachos and Papazachou, 2003).

In search of similarities with previous activity in the study area, it is revealed that instrumental seismicity (since 1900) is mainly located offshore, between Lesvos, Chios Islands and the western coast of Turkey (Fig. 1). Despite the fact that the obtained image by regional earthquake catalogues lacks resolution, given the low detectability of the respective seismological networks (e.g. Mignan and Chouliaras, 2014), more than 120 seismic events with $M_s \geq 4$ have been registered in the broader area since 1900 (Fig. 1) (Makropoulos et al., 2012). In addition, locally recorded microseismicity during 1987–1988 by a temporary network (Delibasis and Voulgaris, 1989; Voulgaris et al., 2004) presented concentration of epicenters on Lesvos Island.

The most recent seismic activity in the broader Lesvos area before the earthquake of 12 June 2017 occurred earlier in the same year, in two regions close to the western coasts of Turkey. The first, at the tip of the Biga Peninsula north of Lesvos (Fig. 1) and the second about 100 km ESE of Lesvos, close to the Turkish city of Manisa. The magnitude of the largest event in the first case was $M_w = 5.2$ (two events), whereas in the second $M_w = 5.1$. According to the results of SL-NKUA, the vast majority of focal mechanisms in both areas reveal normal faulting (Fig. 1), with the causative fault striking in a NW-SE direction. The aforementioned suggest that the east Aegean is a highly hazardous seismogenic region.

In the frame of this work, a comprehensive dataset of recordings from the Hellenic Unified Seismological Network (HUSN), a local temporary network and the Bogazici University Kandilli Observatory and Earthquake Research Institute (KOERI, 2001) was collected and applied towards a detailed investigation of the region's seismotectonics. In this respect, the following are elaborated: (a) determination of precise hypocentral locations by manual analysis of waveform data from all operational stations in the region, employing a custom velocity model, followed by double-difference relocation, (b) spatiotemporal analysis of the sequence to understand the geometry of the activated structures, reveal possible migration patterns, indications of the main rupture's directivity, clustered activity and secondary subsequences, (c) regional moment tensor inversion for the determination of the source parameters of the mainshock and the largest events, (d) inversion of focal mechanisms to investigate the local stress-field and (e) computation of Coulomb stress transfer to identify the nature of the sequence, regions that were loaded with additional stress by the mainshock and their relation to the distribution of aftershocks.

2. The effects of the mainshock

With respect to secondary effects, landslides and surface ruptures caused temporary blockage of the roads. Both road accesses from Plomari closed due to rock falls; the access from Lesvos capital, Mytilene, was also temporarily blocked, in the area of Agios Isidoros, due to landslide of the roads slopes. Severe damage occurred on the provincial coastal road connecting Plomari with Melinta, in the SE part of Lesvos, where rocks have fallen, due to which the access of the road was denied. A small tsunami was generated offshore southeastern Lesvos and was observed in Plomari port, with wave height of 30–40 cm. Blur, vortex, drawback and return of the sea water, as well as characteristic movements of the boats were observed. It is worth noting that no damage was incurred to the tourist infrastructure of Lesvos, fact of crucial importance in view of the current summer season. Only minor problems were reported in Chios Island, where an old house in the Vouno village collapsed, while damage was also reported at a house in Kampos. The tremor was also felt in Istanbul, the western Turkish province of Izmir and in Bulgaria. According to the Turkish emergency management agency, there were no reports of casualties or injuries in the country.

As far as the impact to the built environment of Lesvos is concerned, first considerations are presented based on the preliminary data released by the local Earthquake Rehabilitation Organization (ERO). According to the first degree inspections, conducted few days after the main-shock, the buildings are characterized with respect to their main bearing system/material and immediate habitability. Until presently, inspection data regarding a total of 1996 buildings is available, among which 1143 are tagged as “immediately uninhabitable”. Fig. 2a, presents their distribution with respect to their construction material. It is evident that the most vulnerable typology of load bearing masonry walls has suffered most of the damage. Panel b and c of Fig. 2 summarize the absolute number and the ratio of the habitable and uninhabitable masonry buildings for the most affected localities, respectively. As it can be observed, the largest damage throughout the island occurred in Vrissa, where 436 buildings (64% of the building stock) were heavily affected and around 80% has exhibited some degree of damage. Regarding reinforced concrete buildings, 12 in Vrissa and 7 in Plomari have been characterized as uninhabitable, without yet having further information regarding the type of damage or erection period. Monumental constructions, such as post-Byzantine churches suffered some damage to their structural and non-structural elements.

Based on the preliminary results released by ERO (first order inspection), the macroseismic field of the 12 June 2017 earthquake has been estimated according to the EMS-98 (Grünthal et al., 1998) (Fig. 3). It is noted that, apart from Vrissa, i.e. the locality with the most severe damage, the inspections elsewhere have taken place upon request of each building's owner and, thus, non-complete sampling may impose some effect on the outcome. A range of intensities varying between V and VI is assumed for most of the localities where inspections were either not performed, or revealed only safely habitable buildings. In a forthcoming second order inspection stage, the initially “uninhabitable” buildings will be further distinguished into “Green—Safe for Use”, “Yellow—Unsafe for Use” and “Red—Dangerous for Use” according to the Earthquake Planning and Protection Organization guidelines (EPPPO, 2014). Typically, the last two categories are considered, which incorporate all degrees of damage, from 3 (substantial-to-heavy) to 5 (destruction). Taking into account these assumptions and given that data regarding the actual damage is not yet available, an intensity range has been attributed to the most affected localities. In particular, for Vrissa, the partial collapse of most of the damaged structures leads to the conclusion of local intensity IX.

2.1. The Vrissa paradox

Vrissa settlement was hit the hardest by the earthquake. Being

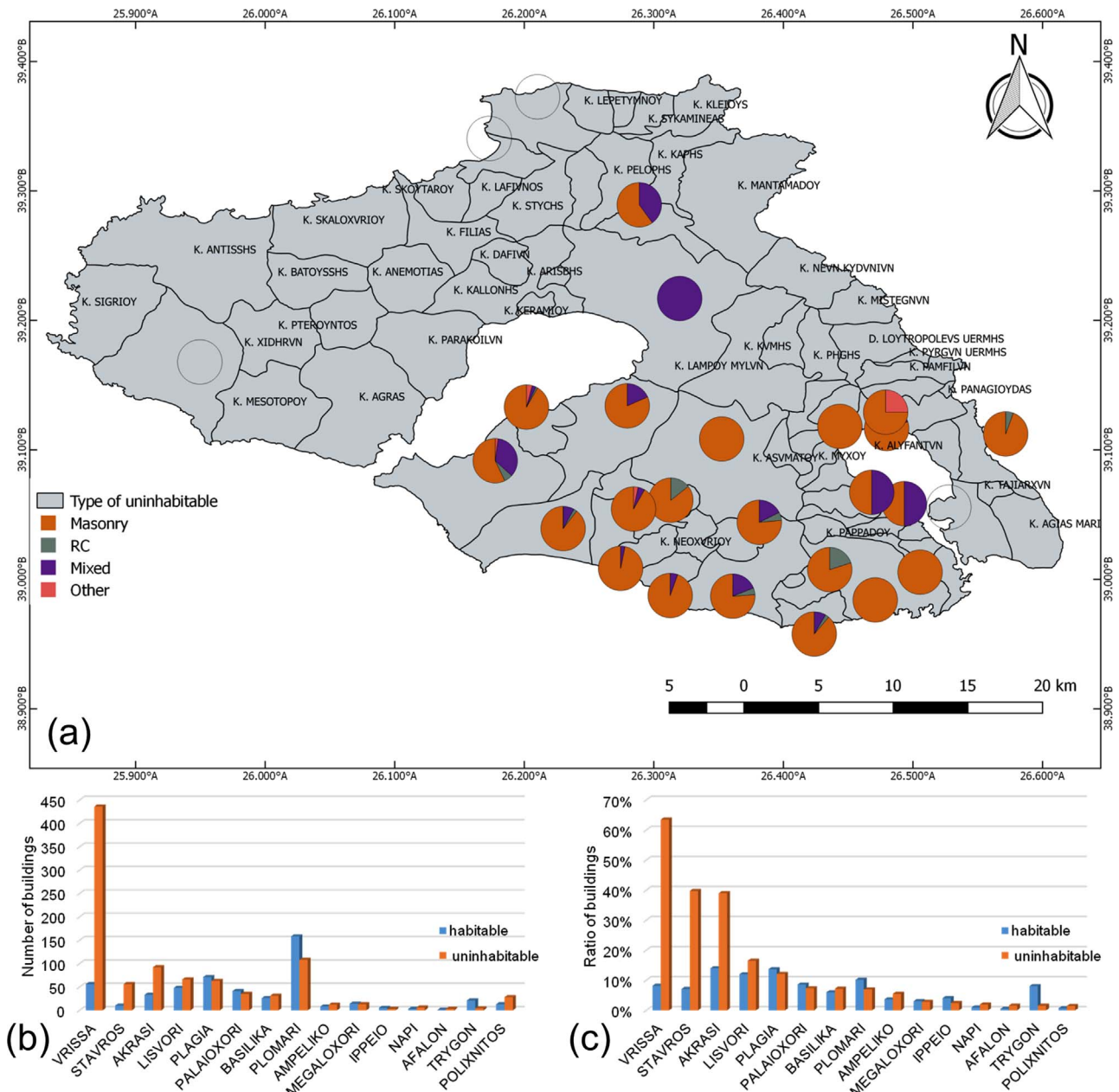


Fig. 2. (a) Distribution of uninhabitable buildings with respect to their construction material, (b) number and (c) ratio of “uninhabitable” masonry buildings based on the latest Census (EL.STAT., 2011).

further from the epicenter than other settlements that suffered much less damage (e.g. Plomari, Vatera, etc), Vrisssa seemed somewhat as an impact paradox. Moreover, the first reports, apart from the fatality and fifteen injuries, referred to numerous collapses and high grade damage. A twofold of activities were performed by our research team during an in-situ survey conducted few hours after the mainshock in Vrisssa: a) a house-by-house inspection of the damaged buildings, upload of their geocoded photos to an online GIS application, so that all interested parties have access to the information and b) construction of a detailed 3D model of the settlement with the use of a UAS (DJI Phantom 4 Pro) and appropriate software (Pix4D), before any intervention was made in the settlement (Antoniou et al., 2017) (Fig. 4).

Most of Vrisssa’s building stock includes stone masonry structures, built during the end of the 19th century or the beginning of the 20th century that were heavily damaged. In order to understand the reasons for this damage distribution in Vrisssa, various factors were taken into account. It is concluded that the geological setting, morphological

parameters, geotechnical properties of the foundation soils and the building characteristics in the devastated village have been identified as factors controlling the spatial distribution of building damage in Vrisssa settlement. More specifically, the existence of old and highly vulnerable structures founded on recent deposits and on slopes in an area that it is bounded by active faults, in combination with directivity and amplification phenomena, resulted in the observed destruction (Lekkas et al., 2017b).

However, there are parts of the village that do not exactly meet these criteria (as for example the school area), that is, the buildings that are not founded on slopes or alluvial deposits. Moreover, there are buildings belonging to vulnerability class (C) that did not suffer the same damage grade, although being in the heart of the mostly hit part of the settlement. Consequently, the above conclusions cannot be easily generalized for the total damage or the whole village and further research is necessary and ongoing.

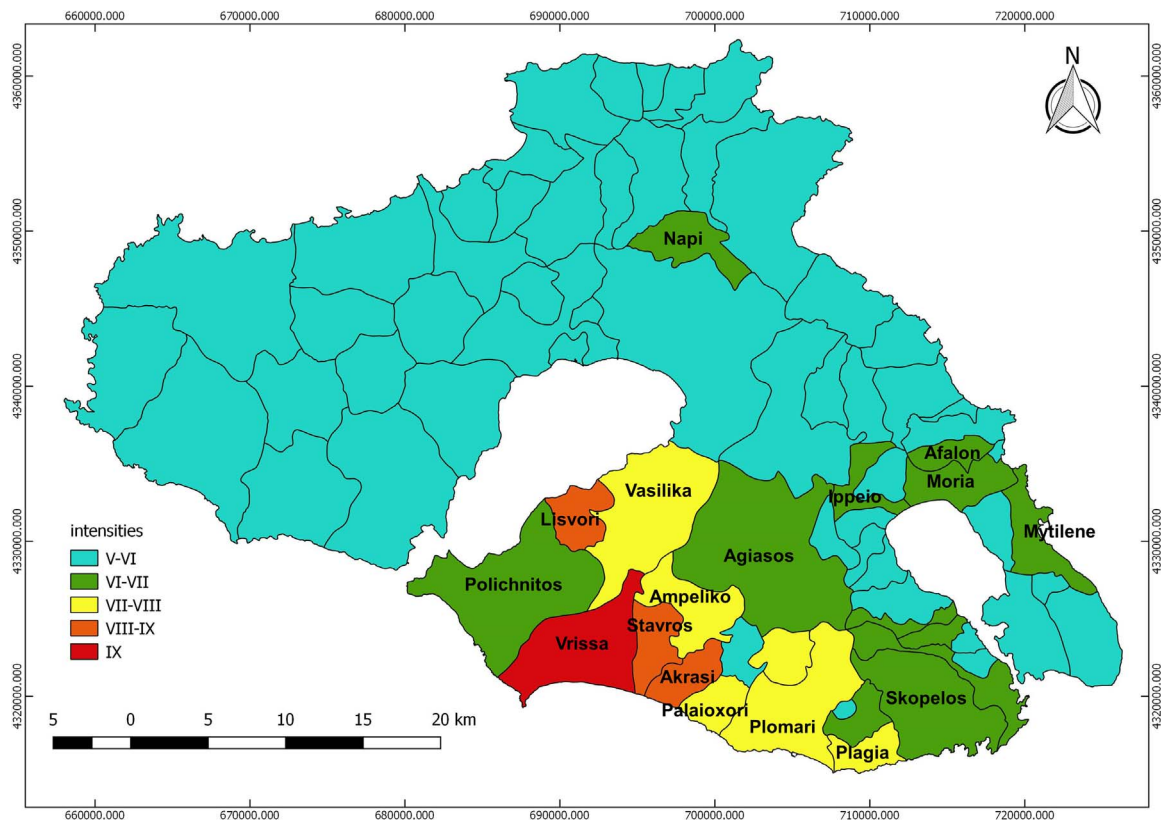


Fig. 3. EMS-98 Macroseismic intensities of the 12.6.2017 $M_w = 6.3$ earthquake.

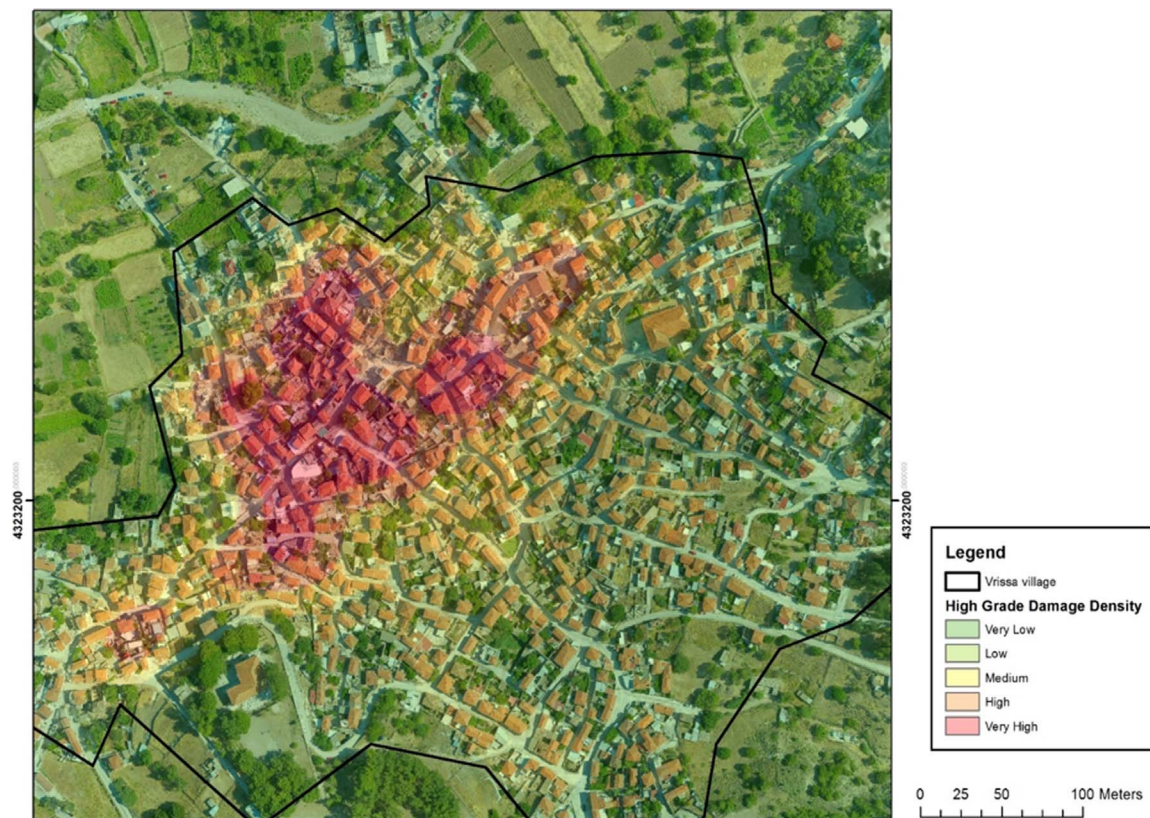


Fig. 4. Damage density in Vrisa village (Lekkas et al., 2017c). Orthophotomap created with Pix4D, with the use of UAS photos one day after the occurrence of the mainshock.

3. Analysis of the aftershock sequence

In the framework of the present study, data recorded by seismographs of HUSN, a virtual network in Greece comprising stations belonging to the SL-NKUA, the Institute of Geodynamics of the National Observatory of Athens (GI-NOA), the Seismological Laboratory of the University of Patras and the Department of Geophysics of the Aristotle University of Thessaloniki, were used. In addition, recordings from three temporary stations, installed in Lesbos and Chios islands by GI-NOA, and from broadband and strong motion stations of KOERI (2001), were incorporated in the waveform database in order to increase the azimuthal coverage and to determine more accurate hypocentral solutions. The waveform data from stations that were not available by HUSN were retrieved through the European Integrated waveform Data Archive (EIDA) node, located in KOERI, via the web services provided by the International Federation of Digital Seismograph Networks (FDSN), facilitating prompt data availability toward monitoring the seismic sequence. Data of the three temporary stations were acquired from the EIDA node of GI-NOA via the ArcLink data request protocol. The closest stations to Lesbos, recordings of which were used herein, are shown in Fig. 1.

3.1. Location of the sequence

P- and S-wave arrival times were manually picked for 915 earthquakes that occurred between 12 and 30 June 2017, given that since 1 July and until presently, the aftershock activity significantly decreased. The initial hypocentral solutions for the study area were determined using a regional velocity model proposed by Karakonstantis (2017). Next, events with at least eight (8) P- and five (5) S-wave phases were employed to obtain a local optimum 1D velocity model for the available dataset. The optimum model was determined by applying the location error minimization method (Kissling et al., 1994; Chiarabba and Frepoli, 1997; Lopes and Assumpção, 2011) and the HYPOINVERSE location algorithm (Klein, 1989). The concluded local velocity model, consisting of seven (7) horizontal homogeneous layers (Table 1), yielded significantly improved hypocentral solutions with respect to the initial regional model (Table 2). The value of the V_p/V_s ratio was obtained using: a) the Chatelain method that consists of determining the slope, using linear regression, of the straight best-fit line of the differences of the P- and S-wave arrival-times for every pair of stations (i, j), $V_p/V_s = (t_{sj} - t_{si}) / (t_{pj} - t_{pi})$, for all events (Chatelain, 1978) and b) the travel-time residuals and location uncertainties errors minimization method. The V_p/V_s ratio value obtained by the application of both methods was identical, equal to 1.79. Magnitudes were determined using the coda duration and an empirical relation that takes into account the duration and the epicentral distance (Kaviris, 2003; Papadimitriou et al., 2010).

The statistics of the hypocentral solutions of the 915 manually analyzed events that were obtained using the determined 1-D velocity model for the study area are presented in Fig. 5. The magnitude values

Table 1
Initial and final velocity model.

Layer	Karakonstantis (2017) $V_p/V_s = 1.79$		Model (This Study) $V_p/V_s = 1.79$	
	V_p (km/s)	Depth (km)	V_p (km/s)	Depth (km)
1	5.1	0.0	5.1	0.0
2	5.4	5.0	5.7	4.0
3	5.9	9.5	6.1	7.0
4	6.0	15.0	6.3	10.0
5	6.5	19.0	6.5	20.0
6	7.0	30.0	7.8	35.0
7	7.3	60.0	8.1	80.0
8	8.1	85.0		

Table 2
Mean location and depth uncertainties for the initial and final models.

	Karakonstantis (2017)	This Study
Mean RMS (s)	0.303	0.235
Mean ERX (km)	1.714	0.756
Mean ERY (km)	2.347	1.110
Mean ERZ (km)	6.538	4.350
Mean Depth (km)	14.387	9.437

reach $M_w = 5.2$, with the majority (87.3%) ranging between $M = 1.8$ and $M = 3.0$. Most focal depths (82.2%) are less than 12 km. The use of the optimal, as previously described, dataset yielded satisfactory horizontal location uncertainties. More specifically, the majority of the epicentral solutions present ERX (99.4%) and ERY (98.8%) less than 2 km. Concerning ERZ, almost all values are smaller than 4 km, whereas RMS mainly ranges between 0.0 s and 0.3 s, with 65.8% of the values being smaller than or equal to 0.2 s.

The Frequency-Magnitude Distribution (FMD) diagram, presented in Fig. 6, shows that the final catalogue is complete down to $M_c = 2.2$. The b -value of the Gutenberg-Richter (G-R) law (Gutenberg and Richter, 1944) is $b = 0.96$ for the linear part of the distribution, or $b_{MLE} = 0.99$ by maximum likelihood estimation. These are higher than the reported background b -value, which according to Papazachos and Papazachou (2003) is $b = 0.84$. It is also higher than $b = 0.85$ that was determined by employing the earthquake catalogue of Makropoulos et al. (2012) and the source zones determined by the SHARE Project (area source TRAS395 of the 2013 European Seismic Hazard Model; Arvidsson et al., 2010; Woessner et al., 2015). This result is consistent with a reduction of the local shear-stresses due to the occurrence of the 2017 mainshock. Furthermore, the extrapolation of the diagram down to $N = 1$ shows that the expected largest magnitude is $m^* \approx 5.13$, which closely matches the one observed for the $M_w = 5.2$ event that occurred on June 17th.

3.2. HypoDD relocation of the sequence

Aiming to further improve the clarity of the epicentral spatial distribution by reducing the relative location errors, the double-difference relocation algorithm HypoDD was employed (Waldhauser, 2001). This method works by minimizing the double-difference between observed and calculated travel-times for pairs of neighboring events and relocates the hypocenters by assuming that if the inter-event distance is much smaller compared to the approximately common ray-path then travel-time differences can be attributed to the inter-event distance. The algorithm can incorporate both catalogue and cross-correlation differential times. The latter can account for arrival-time reading errors and also create links between strongly correlated events.

Cross-correlation measurements of full-signal waveforms (both P and S) were applied on station PRK, which was chosen as a reference station due to its proximity to the epicentral area and its adequate operational status (working continuously since the time of the mainshock without gaps on any component). The waveforms were filtered between 2 Hz and 15 Hz, while all 3 components were taken into account. Cross-correlation was performed between all pairs of resolved events and the respective value of the cross-correlation maximum, XC_{max} , was registered in one matrix per component. Due to the relatively large dimensions of the spatial distribution, with only few apparent spatial clusters, the matrices mainly contain small XC_{max} values with relatively few significant ones. To strengthen the correlation values, the results for all three components were combined by keeping the maximum XC_{max} for each pair from any component. Nearest-neighbor linkage was then applied to construct multiplets, i.e. groups of events with similar waveforms, hence similar focal parameters, after selecting a proper correlation threshold at $C_{th} = 0.64$. The latter was chosen

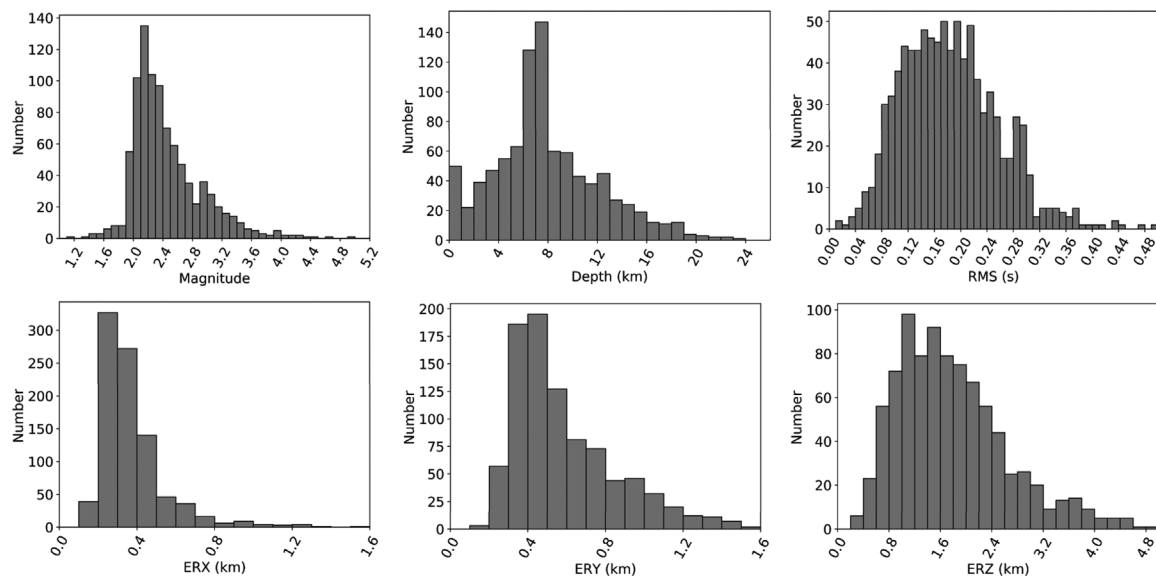


Fig. 5. Histograms presenting the summary of the solutions of 914 manually analyzed aftershocks of the sequence.

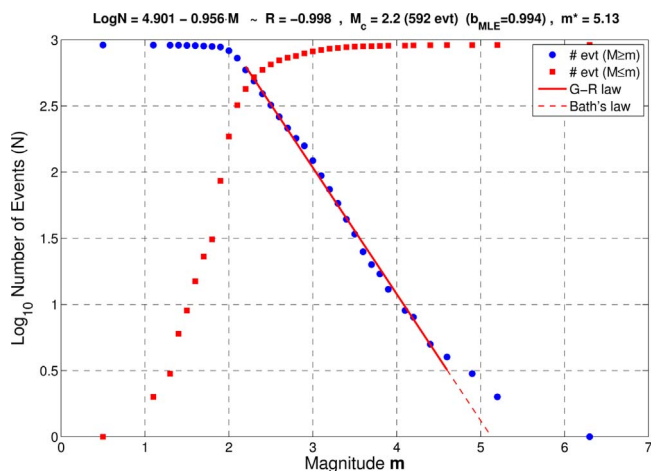


Fig. 6. The FMD of the 2017 Lesvos aftershock sequence. Blue circles and red squares represent the number of events with magnitude $M \geq m$ and $M \leq m$, respectively. The solid red line is the least squares line representing the Gutenberg-Richter (G-R) law. Its extrapolation down to $N = 1$ (dashed red line) marks the expected magnitude of the largest aftershock, m^* , according to the modified Bath's law (Shcherbakov and Turcotte, 2004). (For interpretation of the references to colour in this figure legend, the reader is referred to the web version of this article.)

using an empirical rule, according to which the optimal threshold is the one that maximizes the difference between the size of the largest multiplets and the sum of clustered events (Kapetanidis, 2017). This resulted in 560 events (61%) sorted into 126 multiplets, with 24 of them containing at least 5 events. Cross-correlation measurements were then applied for all pairs of events within each multiplet at all available stations within a 150 km radius from the mainshock, on P- and S-wave windows separately. The time-lag of the resulting XC_{max} was also measured and registered as a differential time measurement along with XC_{max} as weight, to be used as cross-correlation input data for HypoDD.

Relocation was then applied in two main sets of iterations, the first mainly taking into account catalogue data with a small *a priori* weight to cross-correlation data and then reversing the weights relation to improve the relative locations of strongly correlated events. A total of 718 events (78.6%) were successfully relocated. Fig. 7 presents the distribution of the epicenters derived by the HYPOINVERSE (Fig. 7a) and HypoDD (Fig. 7b) procedure. Many sparse events in the HYPOINVERSE locations were shifted towards a few spatial clusters, which

were concentrated into tighter volumes near their centroids, while several outliers, mainly due to the lack of available observations (requiring at least 8) or links within certain margins of inter-event distances and residuals, were rejected. Despite several attempts using different weighting methods, experimental gradient velocity models and station-corrections, the depth estimates could not be significantly improved. Most spatial clusters were found to exhibit a sub-vertical distribution which is indicative of large depth location errors due to the large interstation distances. Nonetheless, the horizontal relocations are considered reliable, especially for clustered events.

4. Moment tensor solutions

Moment tensor inversion was applied using regional waveforms recorded by the HUSN stations. The procedure followed has successfully been applied in several regions of the Greek territory (e.g. Kassaras et al., 2014a; Kapetanidis et al., 2015; Papadimitriou et al., 2015). Waveform data selection criteria were high signal to noise ratio and the optimal, according to the available data, azimuthal station coverage. Data processing involves instrument response correction and bandpass filtering in the range of 0.035–0.200 Hz. Synthetic seismograms were produced using the Axitra code (Bouchon, 1981) for five elementary types of faulting, and the moment tensor elements were calculated using the Singular Value Decomposition (SVD) method (Nash, 1990; Golub and Van Loan, 1996). Finally, a grid search was performed for the estimation of the misfit function of strike, dip, rake and focal depth (Papadimitriou et al., 2012).

Fig. 8 presents two examples of the results of the modelling procedure for the mainshock and the largest aftershock of the sequence. In the first case, the determined focal mechanism, obtained using recordings of 16 seismological stations (6 vertical and 15 horizontal components) revealed normal faulting with strike 122° , dip 40° , rake -83° , centroid depth 13 km and seismic moment $M_0 = 3.5 \cdot 10^{25}$ dyn cm. The solution presents satisfactory fitting between the observed (red) and the synthetic (blue) waveforms for the selected stations, as evidenced by the misfit value (0.15).

Concerning the major aftershock, where 14 stations (7 vertical and 7 horizontal components) were used, the focal mechanism is strike-slip with $\phi = 238^\circ$, $\delta = 68^\circ$, $\lambda = -163^\circ$, centroid depth 11 km and seismic moment $M_0 = 7.8 \cdot 10^{23}$ dyn cm. The results, as evidenced by the misfit error (0.14) and the variance (0.80), are satisfactory. The calculated moment magnitudes of the presented events are $M_w = 6.3$ and $M_w = 5.2$, respectively.

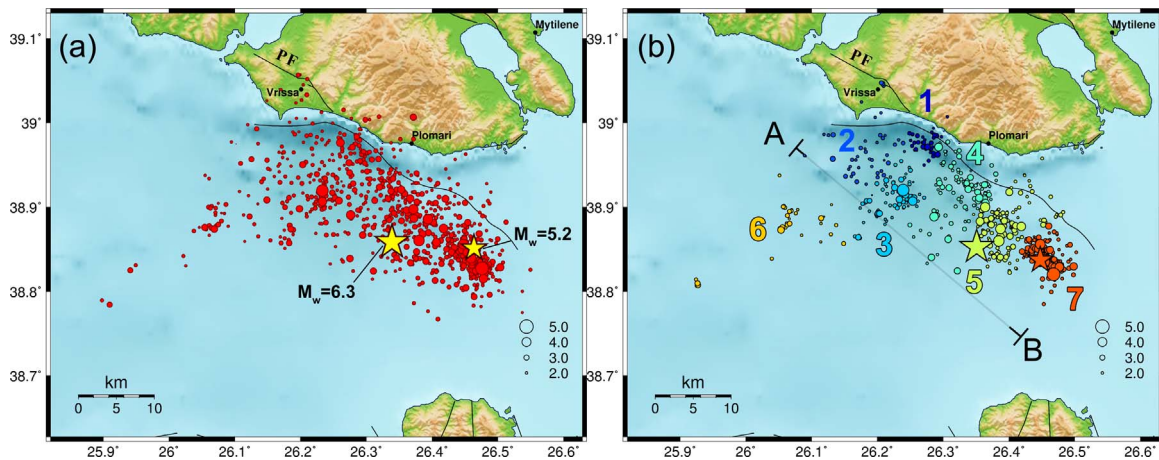


Fig. 7. a) Map of the manually located events of the June 2017 Lesvos sequence. b) Map of the relocated events. Solid black lines denote active faults. The two stars denote the epicenters of the mainshock and the largest aftershock. Colors and numbers in panel b) refer to the 7 spatial groups determined for the relocated catalogue (Section 5). The profile line A–B is used for the spatiotemporal projection of Fig. 11b.

By applying the above procedure, moment tensor solutions (MTS) were determined for 15 events of the sequence (Fig. 9 and Table 3). The vast majority of the MTS were found to exhibit normal faulting similar to the mainshock. Specifically, their strike presents a range of 114°–159°, whereas the dip ranges between 32° and 67°, defining a NW–SE oriented and SW dipping structure. The largest aftershock differs, presenting left-lateral strike-slip faulting, yet with similar strike to the mainshock, also dipping SW. The inferred existence of normal and strike-slip faulting pattern that has also been documented previously in north Aegean (e.g. Ekström and England, 1989; Kiratzi and Louvari, 2003; Kiratzi, 2014; Kassaras and Kapetanidis, 2017) is investigated in the next paragraphs.

5. Spatiotemporal evolution of the sequence

Spatial and temporal analysis of an earthquake sequence can provide clues concerning the geometry of the activated structures, the existence of clustered activity, related to asperities, implications on the directivity of the main rupture and the possible contribution of aseismic

factors, such as creep or fluids diffusion, to the evolution of the sequence (Kapetanidis, 2017). A spatiotemporal projection along the N130°E oriented profile A–B (Fig. 7b) was performed to investigate the nature/driving mechanism of the sequence (Fig. 10b). The temporal axis was divided into 8 periods (a–h), at key-points, marking secondary outbursts of spatiotemporally clustered activity. The on-fault 20km-long area was activated immediately after the mainshock, with most events occurring in group #5 but also to the neighboring groups #3 and #4 (Fig. 10c). Events in groups #1, #2 and #7 started to appear 1, 3 and 7 h, respectively, after the mainshock, while the westernmost group #6 wasn't activated until about 14 June. During periods a–b all major events are concentrated in group #5. This also marks the, so far, easternmost part of the sequence (Fig. 11a,b), indicating that the directivity of the rupture was towards NNW, which could partly explain the disproportional degree of damage observed in Vrissa. Near the end of period b, a few clustered events occurred in groups #3 and #6. In period c, the former cluster was followed by an $M_w = 4.6$ event on 17 June, while a series of smaller events at the beginning of the period, with an $M_w = 4.2$ earthquake on 16 June (Fig. 10b, c), boosted the

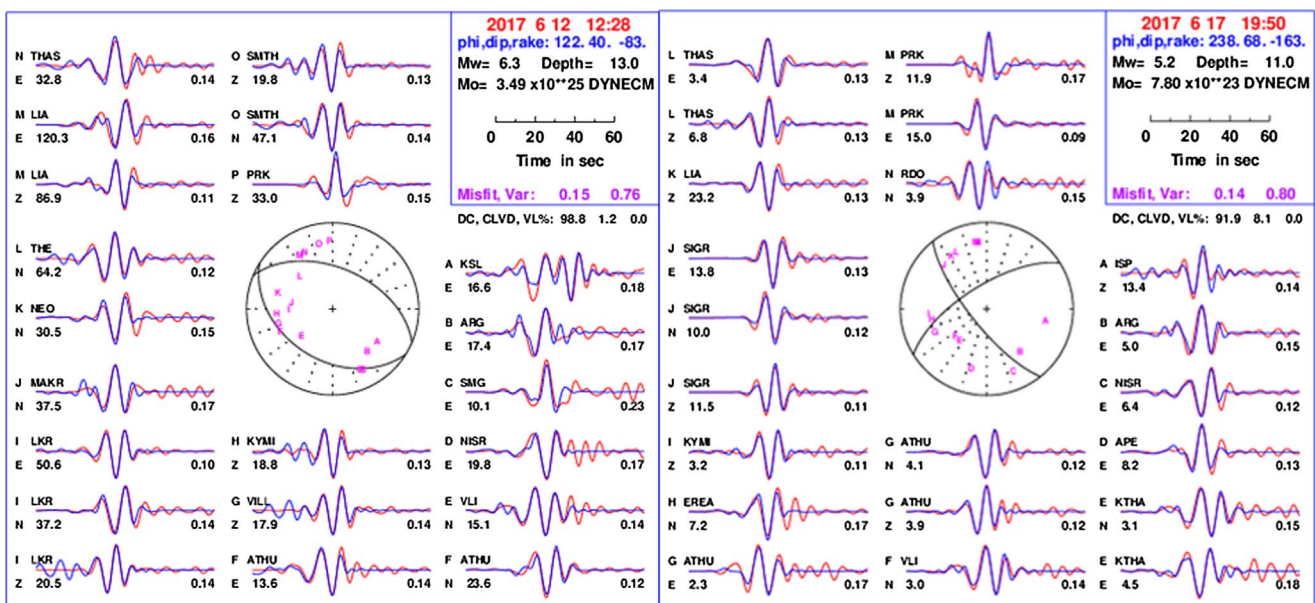


Fig. 8. Focal mechanisms of the 12 June 2017 12:28 GMT mainshock (left) and the strongest aftershock of the sequence at 17 June 2017 19:50 GMT (right), derived by modelling of local and regional waveforms. Synthetic (blue) and observed (red) waveforms and their correlation are presented, for each station. (For interpretation of the references to colour in this figure legend, the reader is referred to the web version of this article.)

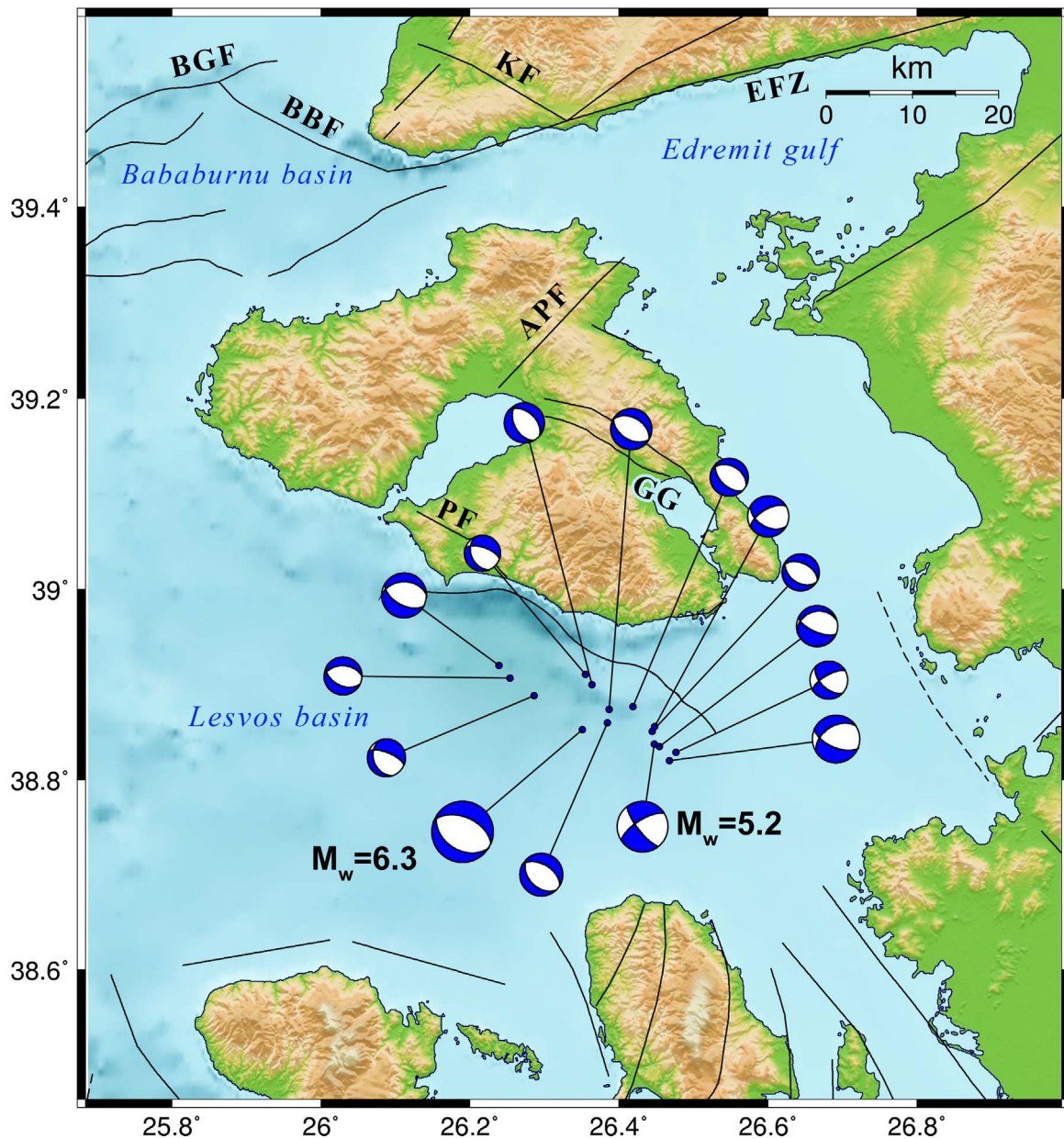


Fig. 9. Focal mechanisms determined for the 2017 Lesvos sequence. Solid black lines denote active faults.

Table 3

Parameters of 15 MT solutions obtained in this study. Epicentral coordinates are after the relocation procedure, whereas focal depths after moment tensor inversion.

No	Yr	Mo	Dy	Hr	Mn	Sc	Lat(°N)	Lon(°E)	Depth(km)	Mag	Strike(°)	Dip(°)	Rake(°)
1	2017	6	12	12	28	38.1	38.8529	26.3509	13.0	6.3	122	40	-83
2	2017	6	12	14	19	47.5	38.8599	26.3848	12.0	4.4	136	41	-78
3	2017	6	12	16	30	15.9	38.8772	26.4189	11.0	3.9	135	52	-80
4	2017	6	12	18	25	41.4	38.8886	26.2863	13.0	3.9	159	32	-47
5	2017	6	13	3	19	59.4	38.8743	26.3871	13.0	4.2	119	47	-91
6	2017	6	14	4	35	56.0	38.9001	26.3639	12.0	4.1	153	48	-75
7	2017	6	15	10	37	4.6	38.9071	26.2539	12.0	3.9	115	48	-74
8	2017	6	16	5	59	22.8	38.9111	26.355	12.0	3.7	156	37	-48
9	2017	6	16	13	25	55.0	38.8561	26.4478	13.0	4.2	120	48	-41
10	2017	6	17	3	40	37.5	38.9203	26.2391	12.0	4.6	119	55	-72
11	2017	6	17	19	33	33.3	38.8352	26.4545	11.0	4.2	114	67	-72
12	2017	6	17	19	50	5.4	38.8375	26.4476	11.0	5.2	142	74	-23
13	2017	6	17	20	16	16.1	38.8509	26.4448	11.0	3.8	124	42	-83
14	2017	6	22	2	48	53.1	38.8204	26.4678	11.0	4.9	114	61	-54
15	2017	6	26	5	54	54.2	38.8291	26.4768	12.0	3.9	134	55	-27

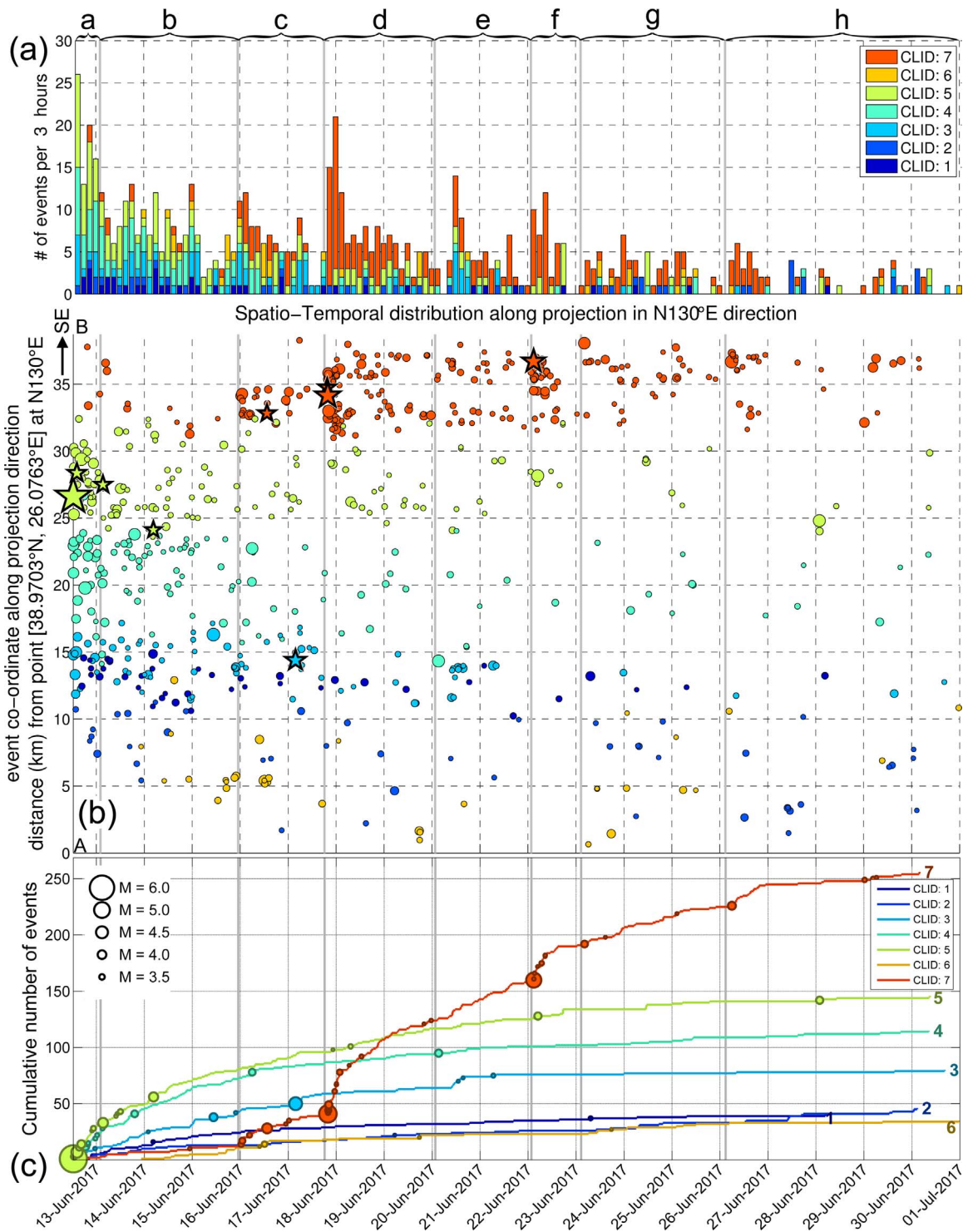


Fig. 10. (a) Histogram of the number of earthquakes per 3 h for the 2017 Lesvos sequence, stacked (colors) according to the respective spatial groups, (b) spatiotemporal projection of the relocated epicenters along the N130°E oriented profile line A–B (Fig. 8b). Stars represent earthquakes with $M_w \geq 4.0$, listed in Table 3, and (c) cumulative number of events for each of the 7 spatial groups. Circles denote major events ($M \geq 3.5$). Vertical thick gray lines divide the 8 successive temporal periods (a–h).

cumulative number in group #7 (Fig. 10c). This likely contributed to the triggering of the largest aftershock ($M_w = 5.2$) that occurred on late 17 June (beginning of period d). In addition, 17 min earlier an $M_w = 4.2$ foreshock (Table 3) was recorded, generating a strong secondary sequence which pushed group #7 at the top of the cumulative number curves by 19 June. The largest aftershock is located roughly in the middle of group #7, oriented NW–SE (Fig. 11d), with activity spreading gradually outwards, towards its margins. While activity in

the other groups was slowly diminishing, with just group #2 exhibiting a small spatiotemporal cluster in period e, group #7 remained highly active, fueled by another major ($M_w = 4.9$) event on 22 June (period e) and some smaller events which, however, generated small sub-sequences of their own at the beginning of periods g and h. Taking into account the gradual spread of activity from the mainshock towards the largest aftershock, an eastwards migration velocity, calculated according to the procedure followed by Kapetanidis et al. (2015), of

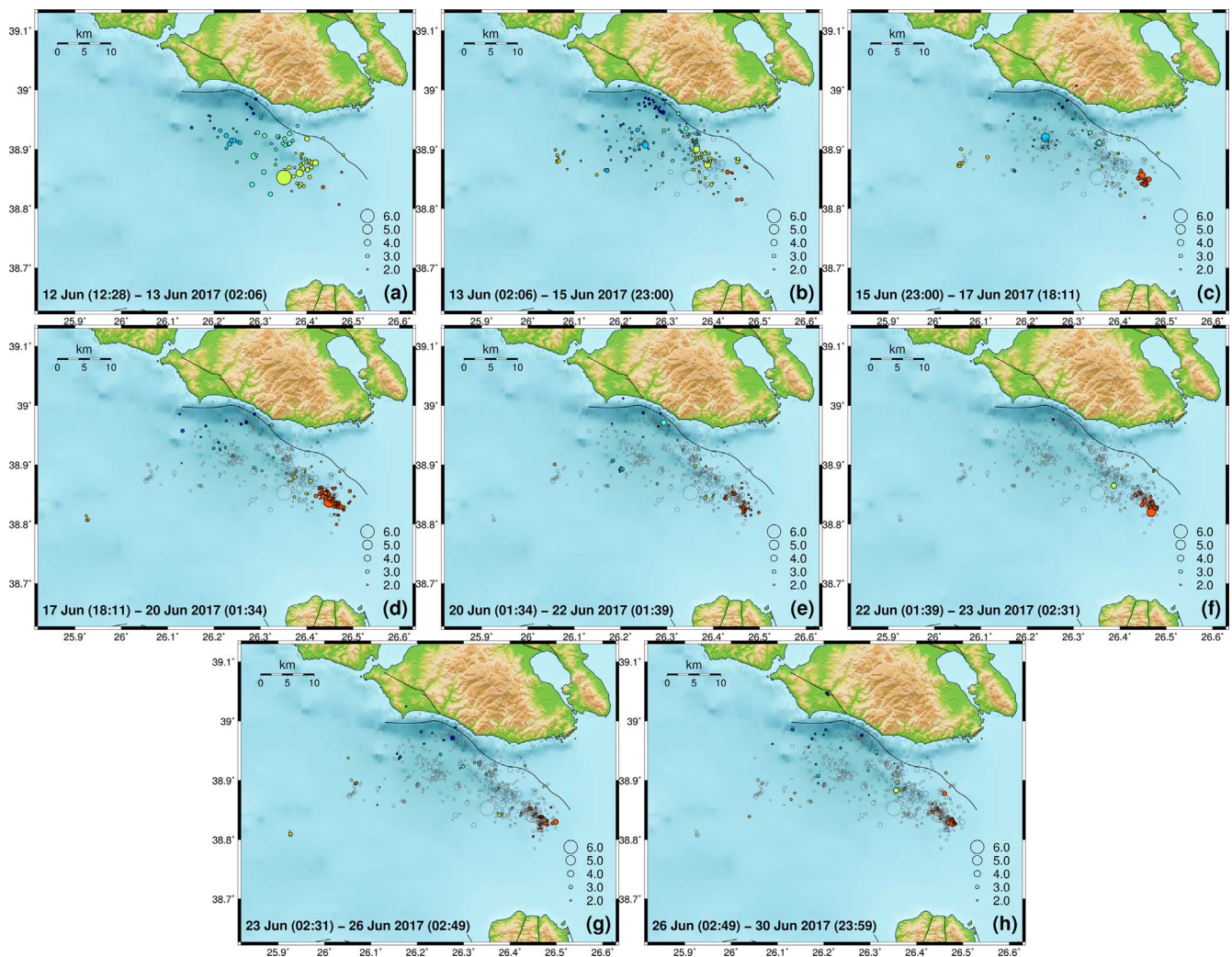


Fig. 11. Maps of temporal evolution of activity during the 2017 Lesvos sequence, divided in 8 periods (a–h). Colors represent the 7 spatial groups. Open gray circles in panels (b–h) represent events that occurred during the previous periods, mainly for spatial reference.

$\sim(1.4 \pm 0.1)$ km/day can be approximated while a roughly $\sim(0.8 \pm 0.1)$ km/day westwards migration velocity can be considered regarding the triggering of the westernmost clusters of group #6. These values are quite large compared to known cases of migration caused by fluids diffusion elsewhere in Greece (e.g. Kassaras et al., 2014b; Kapetanidis et al., 2015), thus they are likely related to tectonic stress transfer, with major earthquakes producing their own subsequences.

Another view of the spatiotemporal evolution of seismicity can be acquired by considering the evolution of multiplets and repeating earthquakes, purely based on the property of waveform similarity (Fig. 12). Naturally, at the beginning of the sequence, given that the mainshock activated a broad area, a large number of new multiplets were abruptly generated, with the largest ones (belonging to groups #4 and #5) during the first 2 days. However, the easternmost group (#7) dominates the multiplets after 16 June, when the occurrence of the largest aftershock on 17 June imposed a culmination of new multiplets, indicating that the activity was spread into non-disturbed regions (e.g. small asperities). The fault patch that was ruptured by the $M_w = 5.2$ event is next to the spatial group where the mainshock belongs, so it may consist an asperity on the same main fault, which is compatible with the delineation of epicenters indicated by the spatial distribution of group #7. This area was likely loaded after the occurrence of the mainshock due to Coulomb stress transfer, a subject that will be investigated in the next section.

6. Implications from stress inversion

Focal mechanisms of earthquakes in the broader Lesvos region were employed in an inversion scheme towards determining the four parameters of the local stress-field in terms of the orientation S_1 , S_2 , S_3 and the relative magnitude σ_1 , σ_2 , σ_3 of the principal components of the tectonic stress tensor, the latter defined by the shape ratio (or shape factor, or aspect ratio, or stress magnitude parameter), R (Gephart and Forsyth, 1984), or Φ (Angelier, 1979, 1984; Angelier et al., 1982; Michael 1984; 1987), related to each other as $\Phi = 1-R$.

For the inversion of focal mechanisms, typically faultless methods are applied. They rely on the W-B assumption (Wallace, 1951; Bott, 1959) for shear stress and slip vector parallelism, the hypotheses of stress uniformity within space and that input focal mechanisms are independent from each other. The main limitations regarding their application on focal mechanism data come from the hypothesis about the stress invariance, which holds when processes that operate at different spatial scales are involved.

The approach of Michael (Michael 1984, 1987) was adopted for resolving the tectonic stress in the study area. It is one of the most acknowledged least-squares stress inversion methods that uses regression to directly determine the best fitting line that minimizes the squares of the deviations between data and model. The data-model misfit in the method is derived by the model confidence regions using a bootstrap technique; for a certain confidence level, a percentage of the

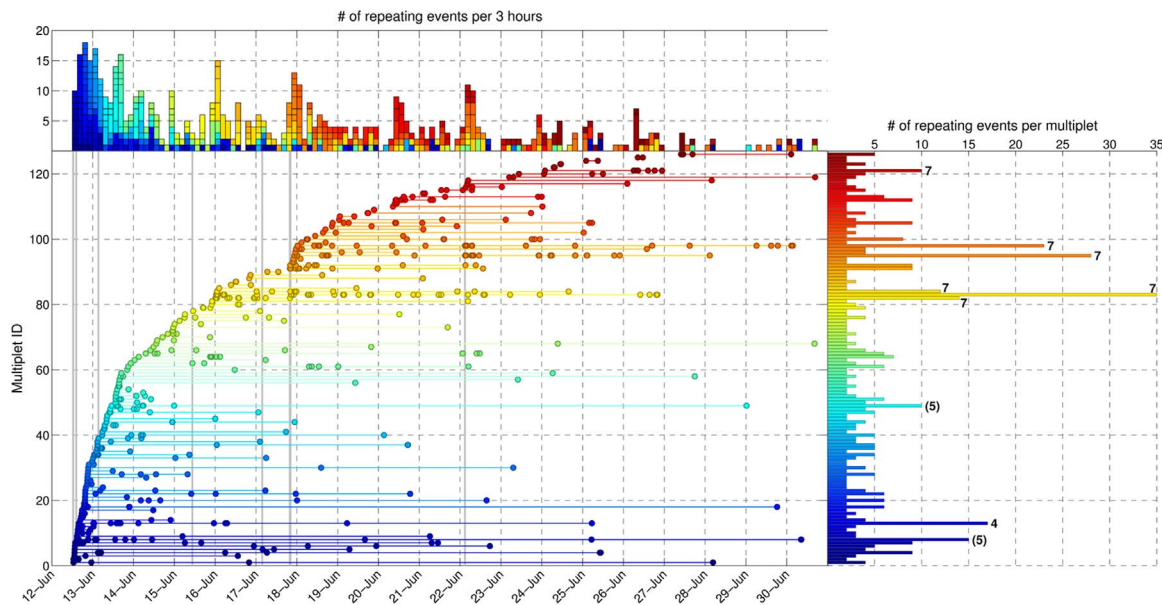


Fig. 12. (bottom-left) Multiplet evolution history during the 2017 Lesvos sequence. Each row represents a single multiplet, with IDs sorted in increasing order according to the origin time of the first event in each multiplet. Circles represent repeating earthquakes. Vertical gray lines correspond to the origin times of major events ($M_w \geq 4.0$), (top) stacked histogram of the number of repeating earthquakes per 3 h, with colors corresponding to the multiplet ID, (right) total number of repeating earthquakes per multiplet. Numerical labels next to certain large multiplets (size ≥ 10) correspond to the spatial groups to which they (mostly; where inside parenthesis) belong.

bootstrap solutions being closer to the preferred solution define the confidence region (Hardebeck and Hauksson, 2001). The SATSI software (Spatial And Temporal Stress Inversion; Hardebeck and Michael, 2006), a variation of Michael's approach, was applied.

Similarly to all faultless methods, inversions in SATSI are conducted within volumes of a small enough size for the assumption of stress uniformity to remain valid. Consequently, the study area is divided in sub-areas and focal mechanisms subsets per sub-region are inverted simultaneously for all cells, searching for the optimal stress within each cell while minimizing the stress differences between neighbouring cells (Hardebeck and Michael, 2006). In SATSI, a damped grid-search is used to optimize the fit between the observed and the calculated stress parameters by minimizing the weighted sum of the data misfit and the model length and to decrease data singularities. Since appropriate damping is needed to produce a regional stress field model that contains only those variations of the stress field that are strongly related to the data, the search for the optimum damping parameter (e) occurs in the first stage of the procedure. The optimum value of e is usually chosen from a range of damping values using the trade-off curve between the data misfit and the model length (e.g. Eberhart-Phillips, 1986). In the second step, stress inversion is performed and the best stress tensors are found for each grid point. In the third stage, the uncertainty is provided by the computation of the confidence interval for each grid node using a bootstrap procedure.

The data set used consists of 82 focal mechanisms with magnitudes ranging from 3.3 to 7.0, available from the comprehensive catalogue of Kassaras et al. (2016) and fault-plane solutions from the SL-NKUA (<http://www.geophysics.geol.uoa.gr>). Fig. 13 illustrates the spatial distribution of the 82 individual focal mechanisms in terms of sense of faulting according to the rake of one of their nodal planes and Table 3 and Table A2 (in Appendix A) present their detailed parameters.

Fig. 13 demonstrates that the focal mechanism data mostly exhibit normal faulting (rake $\approx 90^\circ$). However, more than one type of faulting is inferred at certain areas and spatial sampling inhomogeneity is observed, with some areas having more data than others. The above imply for a varying stress state that probably applies at different scales. In order to correctly reconstruct the stress tensor, given that the inversion is expected to resolve its uniform part only if it is larger than the variable part (Michael, 1991), the data were divided into subsets according to their spatial distribution.

6.1. Application of SATSI

SATSI was implemented using the MATLAB based MSATSI visualization and plotting tools of the inversion results (Martínez-Garzón et al., 2014). The inversion of the 82 focal mechanisms was performed using both nodal planes of focal mechanisms over a 0.5° by 0.5° grid (Fig. 13). The optimum damping parameter (e) was found equal to 1.2 in the first stage of the procedure. Adopted solutions of the inverted model lie within the 95% confidence interval of 2000 resamples, as determined by the bootstrapping method (Hardebeck and Michael, 2006).

Fig. 14 illustrates the results of the SATSI procedure and Table 4 summarizes them. Fig. 14a (95% confidence regions of 2000 bootstrap resamples) provides a measure of the data homogeneity, showing that S_3 axes (red dots in Fig. 14a) present a stable, well-defined solution with respect to the input data. The latter is partly true for S_2 (green dots in Fig. 14a), whereas S_1 (blue dots in Fig. 14a) exhibits large variability, especially at the southern part of the area, including the epicentral area of the June 2017 earthquake sequence.

From Fig. 14b it can be observed that extensional tectonics prevails in the area, with S_3 being almost horizontal in a NNE-SSW direction, compatible with the regional kinematics (e.g. Kreemer et al., 2014). S_1 is less pronounced, oriented in a roughly WNW-ESE direction, thus producing a horizontal sense of slip on the regional fault sources (Fig. 14c), dextral when a NE-SW or an E-W nodal plane is selected as the fault plane, according to the active faults in the area (Ganas et al., 2013) and the broader area's kinematics related to the prolongation of NAFZ in the Aegean (e.g. Armijo et al., 2003).

The pattern of the resolved stress (Fig. 14b, c), implies for more than one stress states involved in the local stress field. However, the SATSI method does not ensure independency of focal mechanism observations, given that it treats heterogeneous data as noise (e.g. Gephart and Forsyth, 1984; Michael, 1984), and hence the method cannot resolve multiple stress states in the presence of heterogeneous data, due to over-smoothing that the damping procedure can induce, and, moreover, because the proper spatial arrangement of focal mechanism datasets is subjective (Kassaras and Kapetanidis, 2017).

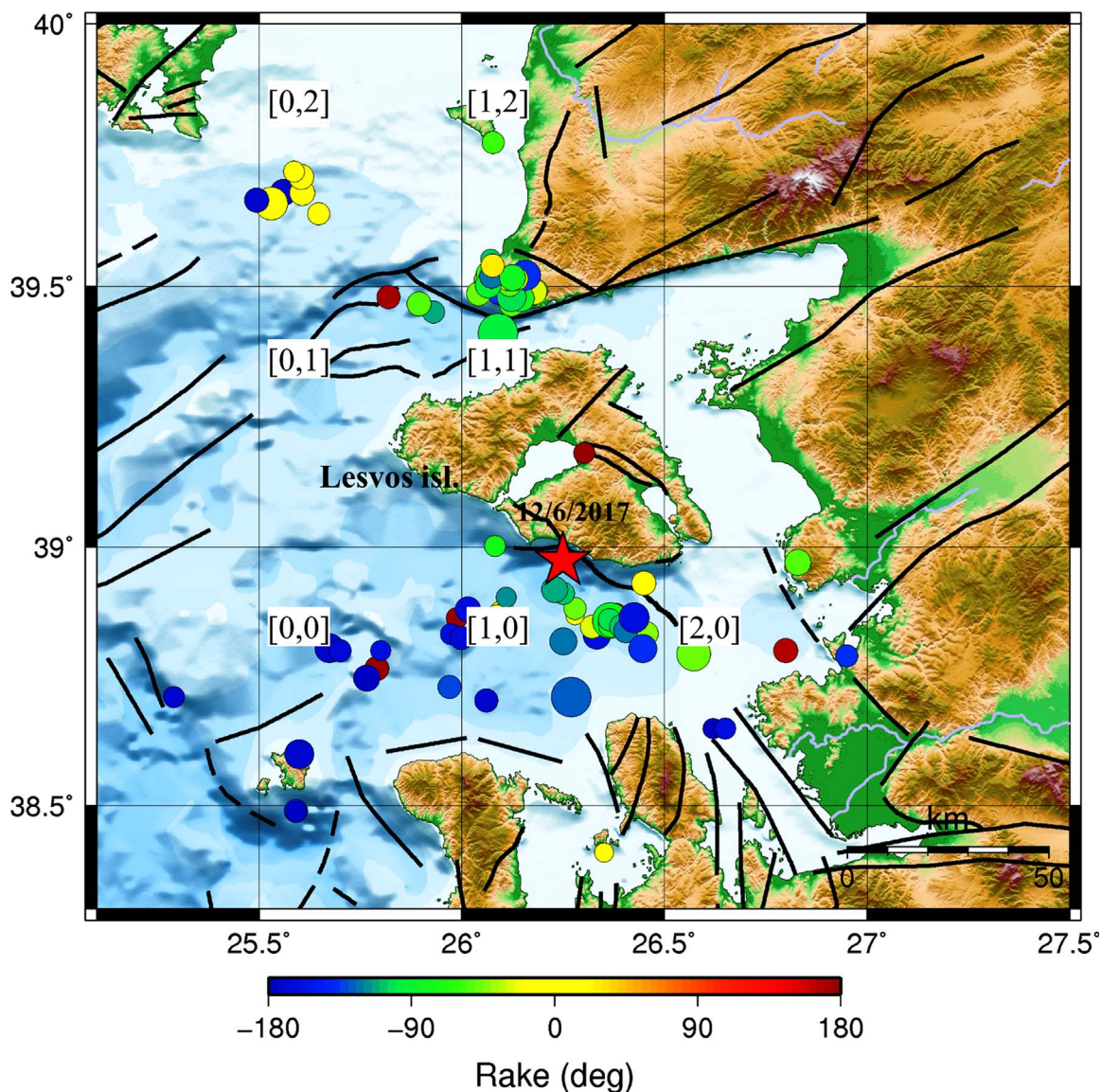


Fig. 13. Spatial distribution of 82 epicenters (circles) of events with focal mechanism data (Kassaras et al., 2016 and references therein; <http://www.geophysics.geol.uoa.gr>) employed in the SATSI inversion scheme. Solid black lines denote active faults. Numbers in brackets denote the coordinates of equal-area sub-regions in which the area has been divided.

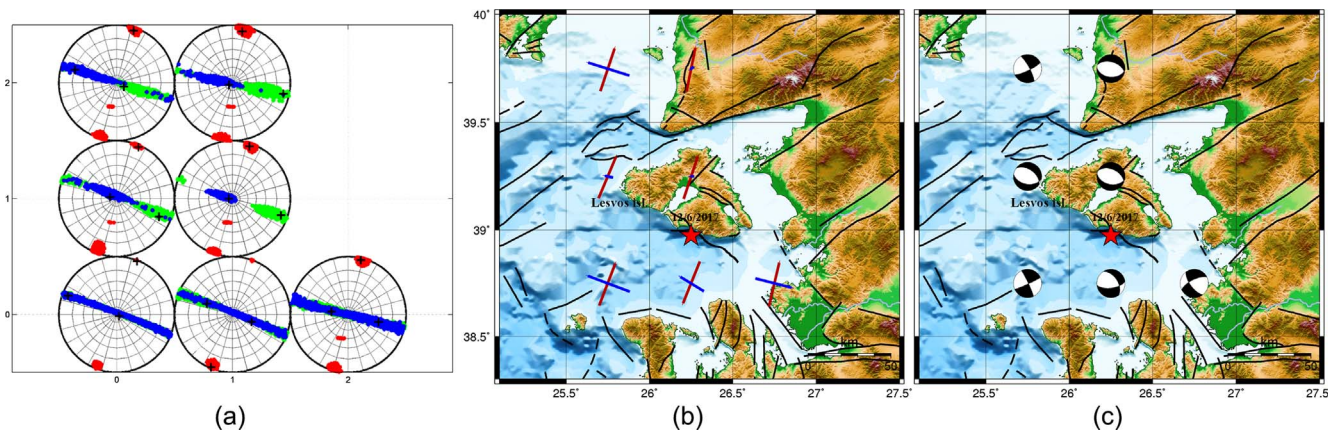


Fig. 14. Results of the MSATSI inversion for 7 sub-regions in the broader Lesvos region. (a) Stereo plots showing the 95% confidence regions of 2000 bootstrap resamples for the S_1 (blue), S_2 (green) and S_3 (red) axes, (b) arrangement of the projections on the horizontal plane of the resolved best-fit principal stress components S_1 and S_3 . The star denotes the $M_w = 6.3$ earthquake that occurred on 12 June 2017 and (c) equivalent focal mechanisms representation of the resolved stress field. (For interpretation of the references to colour in this figure legend, the reader is referred to the web version of this article.)

Table 4
Summary of the stress parameters resolved by the SATSI procedure. FMS: Focal Mechanism Solution.

Sub-region	R	S ₁ trend (°)	S ₁ plunge (°)	S ₂ trend (°)	S ₂ plunge (°)	S ₃ trend (°)	S ₃ plunge (°)	FMS			# FMS
								Strike (°)	Dip (°)	Rake (°)	
[0,0]	0.01	291	6	124	84	21	1	65	86	-176	12
[0,1]	0.14	283	77	113	13	23	2	100	44	-109	4
[0,2]	0.11	288	16	119	74	18	3	64	79	-169	7
[1,0]	0.16	301	51	293	39	202	1	327	50	-37	26
[1,1]	0.21	268	83	109	7	18	3	101	43	-100	11
[1,2]	0.17	238	82	102	6	11	6	95	40	-99	12
[2,0]	0.12	104	33	281	57	13	2	143	66	-24	6

6.2. Application of MIM

Given the above mentioned limitations related to the inversion method and the data configuration (faulting type heterogeneity, spatial sampling, and subjective selection of datasets) and in order to investigate in more detail the local stress field, the MIM (Multiple Inverse Method) (Yamaji, 2000) was applied in the epicentral area south of Lesvos (cell [1, 0] in Fig. 13), which presents high degree of heterogeneity. MIM is a broadly implemented procedure, since it has been proven powerful enough to separate stresses from heterogeneous fault slickenside and focal mechanism data (Otsubo et al., 2008). The method employs a resampling technique (Otsubo and Yamaji, 2006; Otsubo et al., 2008; Yamaji and Sato, 2011) producing *k*-fault subsets from a given set of data, and calculates the optimal stress for each subset by applying iteratively the Angelier’s (1979) inversion scheme. Thereafter, each focal mechanism that belongs to a subset is evaluated towards a set of trial reduced stress tensors using the angular misfit between the observed and the theoretical slip directions and tensors which are more compatible with the data of the subset are considered as optimal (Yamaji et al., 2006).

The MIM procedure comprises the following steps: (a) removal of obsolete nodal planes that correspond to similar focal mechanisms and do not contribute to the solution (Otsubo et al., 2008), (b) rejection of subsets that surpass the $\Delta T = 20^\circ$ misfit angle threshold for any possible stress configuration (Otsubo et al., 2008) and (c) a procedure that employs a user-defined “enhance factor” (EF) to thin out erroneous solutions and enhance correct ones (Yamaji, 2000). Each *k*-th datum is projected on the surface of a unit hypersphere in a five-dimensional Euclidean space, representing five parameters that define the reduced stress tensor (orientation of the principal stress axes S₁, S₂ and S₃ with respective magnitudes σ_1 , σ_2 and σ_3 and stress-ratio Φ) and the fault-slip (Otsubo et al., 2008).

MIM was applied on the focal mechanisms dataset belonging to the epicentral area of the 2017 Lesvos earthquake (grid [1, 0] in Fig. 13), comprising 26 focal mechanisms, most of which correspond to its aftershocks. The method considers both nodal planes of the focal mechanisms to account for the fault/auxiliary plane ambiguity. Resampling of the focal mechanisms for generating subsets was performed using an integer called “data combination number” that controls the number of resamples with respect to the number of input data (Yamaji and Sato, 2011). A value of $\kappa = 5$ was utilized, as suggested by Yamaji et al. (2006) for focal mechanism data.

Figs. 15 and 16 present the results of the MIM analysis. In Fig. 16, observations are plotted as “tadpole” symbols (5-elements stress tensors) on the 5D hypersphere. Significant stresses in the focal mechanisms dataset can be identified graphically as clusters of tadpoles with similar color (Φ or *Phi*), tail direction and tail length. Fig. 15a presents all *k* subsets after the removal of obsolete nodal planes and rejection of subsets with misfit angles $> 20^\circ$. Fig. 15b and c present the distribution of tadpoles “filtered” by the stress shape Φ . Two clusters of stresses are evidenced by Fig. 15, the first (A) having sub-vertical S₁ and S₃ almost horizontal and the second (B) presenting oblique-to-sub-horizontal S₁

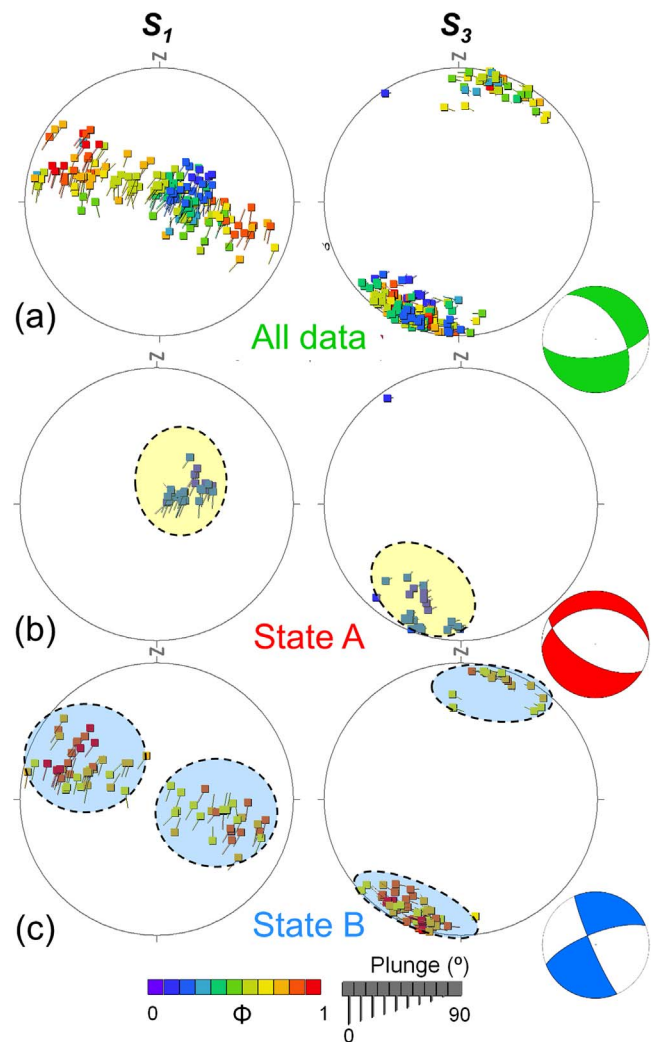


Fig. 15. Stereograms presenting the projection of optimized diagrams of tadpole symbols for S₁ and S₃ after declustering and removal of erroneous data, including (a) all data, (b) data filtered by bluish Φ and (c) data filtered by yellowish-to-redish Φ (or *Phi*). The S₁ tadpole tails indicate the azimuth and plunge of the corresponding S₃ vector and vice versa for the S₃ tail. Colored areas indicate *k*-means clusters characterized as stress states A (yellow) and B (blue). Beach-balls indicate Andersonian style of faulting per each dataset. (For interpretation of the references to colour in this figure legend, the reader is referred to the web version of this article.)

and almost horizontal S₃.

Panels a and b of Fig. 16 present the quality estimates of the resolved stresses by the MIM; stress state A is well explained by the majority of individual observations in terms of their misfit angle with the resolved fault-slip, whereas stress state B appears compatible with a smaller number of observations which present large dispersion across the hypersphere, likely related to the heterogeneity of the input dataset.

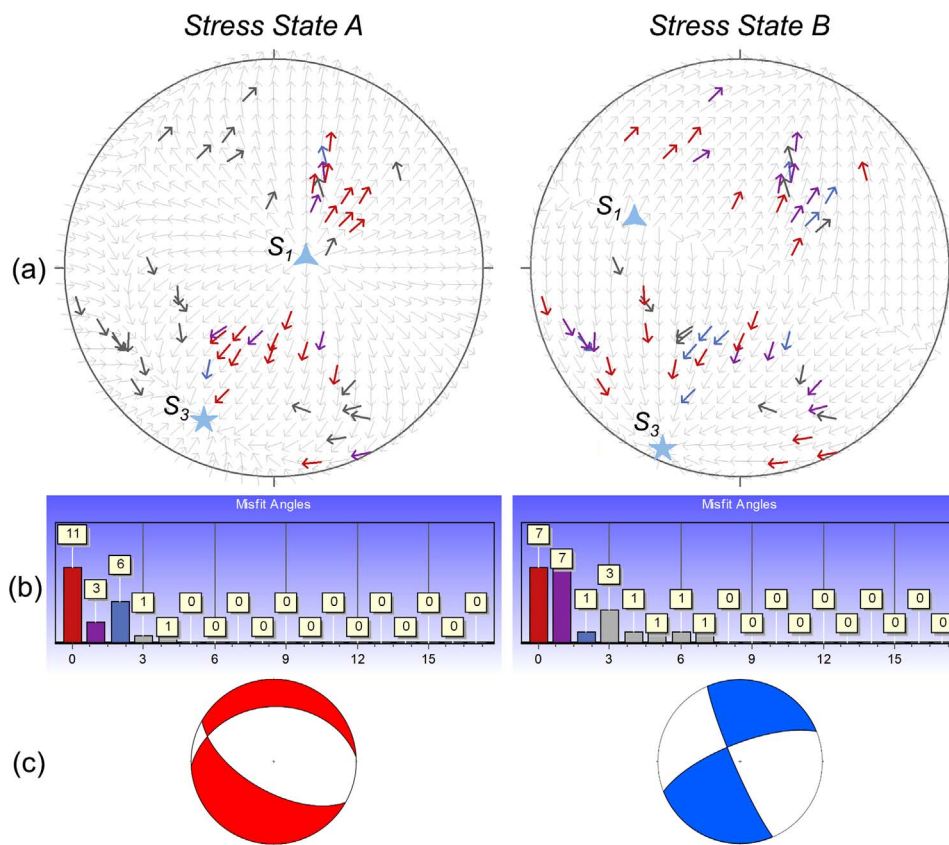


Fig. 16. (a) Diagrams showing tangential-lineation of the input data, color-coded with respect to the misfit angles shown in panel b. Thin gray arrows denote fault kinematics predicted by the resolved stress states, (b) histograms presenting the data-model misfit angles in terms of the slip vector orientations. The horizontal axis is in tens of degrees. The vertical axes denote the multitude of reduced stress tensor pairs with the corresponding misfit value and (c) beach-balls representative of faulting that corresponds to the resolved stress states A and B.

Table 5
The two stress states resolved for cell [1, 0] in the epicentral area. FMS: Focal Mechanism Solution.

Node	Lat (°N)	Lon (°E)	Stress state A					Stress state B				
			S ₁ (°)		S ₃ (°)		Φ	S ₁ (°)		S ₃ (°)		Φ
			Trend	Plunge	Trend	Plunge		Trend	Plunge	Trend	Plunge	
			FMS 1 Strike (°)		Dip (°)		Rake (°)	FMS 2 Strike (°)		Dip (°)		Rake (°)
[1,0]	38.75	25.75	66	69	197	14	0.17	111	17	204	8	0.98
			120		61	-62		249	67	-173		

Table 6
Source parameters by use of the Coulomb v3.3 software (Toda et al., 2011).

M _w	Fault length/width (km)	Fault Top/ Bottom (km)	Depth (km)	Source			Poisson Ratio	E (bars)	μ
				Strike (°)	Dip (°)	Rake (°)			
6.3	18.75/11.8	9/17	13	122	40	-83	0.25	8E + 05	0.4

Nonetheless, both resolved stress states are considered representative of the complexity of the local stress field, consistently with Kassaras and Kapetanidis (2017), who found a similar stress field in the north Aegean region. Normal faults in a WNW-ESE direction are compatible with the orientation of S₁ that characterizes north Aegean. Table 5 summarizes the outcome of the MIM procedure.

7. Coulomb stress transfer

The inferred complex stress state in the epicentral area demands the examination of whether the main-shock may produce triggering to neighboring structures by stress transfer. To this end, static stress change associated with the coseismic slip of the M_w = 6.3 earthquake

was determined on optimally oriented planes related to the deduced local stress state, on the basis of the Coulomb failure criterion (King et al., 1994; Stein, 1999). Coulomb stress is a measure of the increase or decrease of the failure stress on a fault surface, considered to be receiving the energy transmitted by a nearby seismic source. In this respect, positive stress transfer on a receiver fault enhances its rupture, while negative one delays it.

Coulomb stress change was calculated according to the faulting type of the mainshock that has been determined herein by moment tensor inversion, assuming uniform slip. The source fault geometry, as well as the values of Young modulus (E), Poisson's ratio and friction coefficient (μ), involved in the Coulomb stress calculations, are listed in Table 6. The receiver faults were considered according to the local stress field

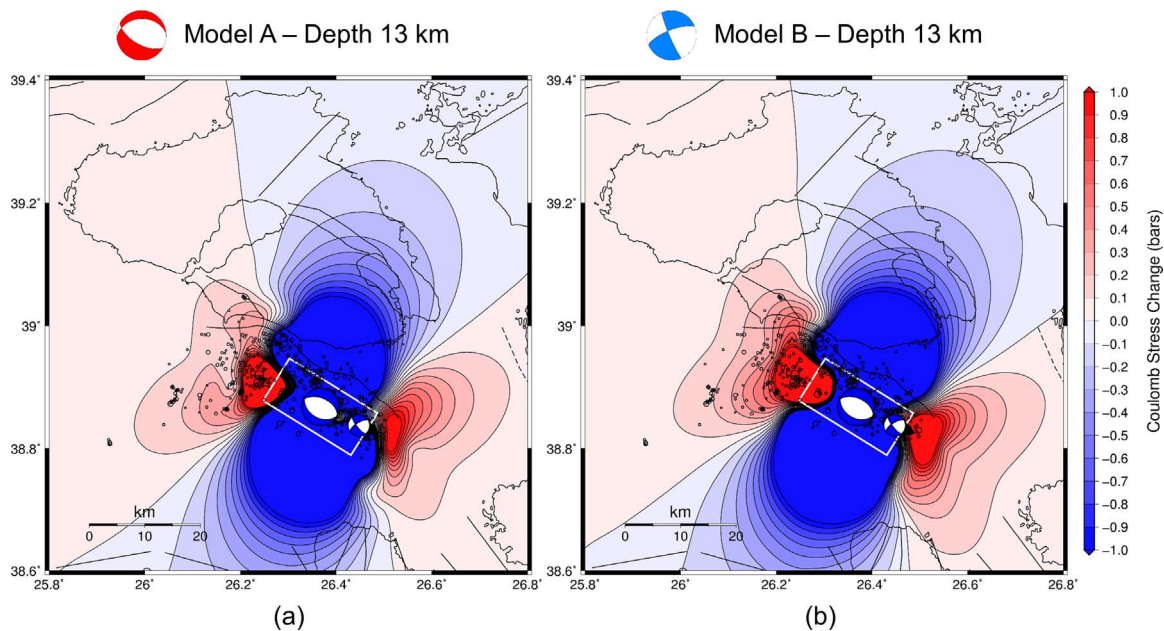


Fig. 17. Coulomb stress change from the $M_w = 6.3$ Lesvos earthquake calculated at 13 km depth on optimally oriented planes according to the regional stress states A (panel a) and B (panel B), respectively (see Table 5). Palette of stress values is in the range -1 to $+1$ bar and contours are per 0.1 bar. Blue and red colors indicate stress unloading and loading, respectively. Black dots denote relocated aftershocks. White rectangle is the surface projection of the ruptured plane. On-fault beachballs indicate the mainshock and the largest aftershock. The beach-balls at the top of both panels represent Andersonian faulting due to stress states A and B (Table 5). (For interpretation of the references to colour in this figure legend, the reader is referred to the web version of this article.)

for two stress states determined in the epicentral area by the previously described focal mechanisms inversion (Table 5).

Fig. 17 presents two models of Coulomb stress transfer calculated on optimal receiver faults based on: (a) an extensional stress regime (model A in panel a) and (b) a strike-slip regime (model B in panel b). It is evident that the 2017 mainshock imposed a lobe of positive static stress at both edges of the causative fault. The on-fault aftershocks are located inside an area of negative stress changes, given that a uniform slip rupture model was considered. The majority of aftershocks is included in the positive lobes (red colors in Fig. 17) at the tips of the fault plane. In this regard, both models, presented in Fig. 17, explain the evolution of the aftershock sequence. However, high stress, predicted by model B (optimal receiver faults based on a strike-slip regime) to have been transferred to the east of the causative fault, better explains the occurrence of the largest $M_w = 5.2$ aftershock on 17.6.2017 for which a strike-slip focal mechanism has been determined (Fig. 8).

8. Discussion—conclusions

On 12 June 2017 (12:28 GMT) a destructive earthquake occurred offshore, approximately 15 km south of the SE coast of Lesvos Island, NE of Chios, causing one fatality, 15 injuries and severe structural damage, mainly in Vrissa village. This event was one of the largest that have occurred in the vicinity of Lesvos Island since the antiquity, as well as during the 20th century.

In this paper, in an attempt to highlight: (a) the nature and dynamics of the earthquake sequence, (b) the driving forces that acted during its evolution and (c) potential consequences of its occurrence on the regional hazard, we present the results of detailed analyses involving assessment of the earthquake effects on the natural and built environment, manual location and relocation of the aftershock sequence, computation of the moment tensors of the largest events, the study of the spatiotemporal distribution of aftershocks, stress inversion and Coulomb stress transfer computations.

Manual data analysis, based on a comprehensive dataset of earthquake waveform recordings regarding the period from 12 to 30 June 2017, led to the location of 915 events, while the application of the

HypoDD algorithm (Waldhauser, 2001) resulted in 718 relocated events with reduced errors. The horizontal spatial distribution of the aftershocks reveals concentration offshore, south of the SE coasts of Lesvos Island. The epicenters are aligned along an approximate NW-SE direction. Regional moment tensor inversion of the major events of the sequence mainly indicate predominant normal faulting, defining an offshore NW-SE oriented and SW dipping plane, related to the Lesvos Basin, where the major part of the aftershocks was concentrated.

The available dataset, even though optimum, did not allow precise determination of the depth distribution of the sequence due to large distances between the epicentral area and the existing recording stations. Given the high seismic hazard of the region, for which identification and detailed investigation of the major offshore seismogenic features is required.

The spatiotemporal analysis revealed a 20 km fault length that was coseismically activated with the occurrence of the 12 June 2017 $M_w = 6.3$ main event. Seismic activity gradually migrated NW of the mainshock and then SE, at a rate that is consistent with stress-related aftershock generation (Fig. 10). A strong subsequence was generated by the largest aftershock ($M_w = 5.2$) of 17 June, at a cluster in the easternmost portion of the spatial distribution (Fig. 10). Thereafter, towards the end of the study period, the activity slowly decreased.

Inversion of 82 focal mechanisms yielded prevalent NE-SW extension, in good agreement with regional kinematics deduced from geodesy (e.g. Kreemer et al., 2014). A complex stress field is inferred south of Lesvos, capable of producing \sim E-W normal and strike-slip faulting. A similar pattern, i.e. coexisting normal and strike-slip faulting is inferred in the north Aegean region from earthquake focal mechanisms (e.g. Ekström and England, 1989; Kiratzi and Louvari, 2003; Kiratzi, 2002, 2014; Kassaras and Kapetanidis, 2017), as well as from kinematic analysis of faults (Aktar et al., 2007) and has been attributed to pull-apart basins at the tips of conjugate strike-slip faults (e.g. Ganas et al., 2005).

Static stress transfer was computed for a uniform slip source model on optimum receiver faults according to the derived local stress field. The distribution of positive stress lobes of both stress states explains well the aftershocks to the western part of the area, whereas the strike-

slip kinematics better explains the largest aftershock of $M_w = 5.2$ located east of the mainshock (Fig. 17). Interestingly, the western positive lobe covers well the south-westernmost cluster (group #6 in Fig. 7b) that was activated on 14th of June, about two days after the occurrence of the mainshock, implying triggering due to static stress load.

Static stress transfer employing all major events in the North Aegean during the post-1943 period on optimal planes to regional compression does not clearly relate to the current crisis, since positive stresses were found only marginally to the activated area. Similarly, Leptokaropoulos et al. (2014) found low static stress changes due to the 6 November 1992 ($M_w = 6.0$) earthquake, that occurred south of Lesvos, producing low positive stresses at the June 2017 epicentral area that possibly did not strongly affect the occurrence of the mainshock. On the other hand, Nalbant et al. (1998) suggest that large historical earthquakes in the area are likely related to stressing the area of south Lesvos.

In conclusion, the 12 June 2017 earthquake, with seismic moment $M_0 = 3.5 \cdot 10^{25}$ dyn cm, ruptured an offshore NW-SE trending normal fault ($\varphi = 122^\circ$, $\delta = 40^\circ$ and $\lambda = -83^\circ$) with a length of approximately 20 km. The mainshock has similar characteristics with the historical earthquake that occurred in 1845. The distribution of the earthquake effects in Vrissa is related mainly to strong site-effects that demand extensive investigation before reconstruction begins, but also possibly to directivity effects of the main rupture. The aftershock sequence is

well explained by static stress load by the mainshock that triggered seismicity to the western edge of the epicentral area. Specifically, apart from the existence of seismicity along the main fault, at the western edge the activity appears prolonged to the SW that could be related to a NE-SW oriented offshore structure. The latter has a similar orientation with the APF which likely produced the 1867 earthquake onshore Lesvos. Nevertheless, further investigation is needed to examine a possible relation between these structures, fact that could be proven of significant importance for seismic hazard assessment of the region. The mainshock has also loaded with stress the eastern part, close to the Turkish coast where major structures related to past strong earthquakes occur.

Acknowledgements

We would like to thank the scientists and personnel who participated in the installation or maintenance of the permanent and temporary stations belonging to the HUSN network. We are grateful to the Observatories and Research Facilities for European Seismology (ORFEUS) and EIDA for the infrastructure that made possible the retrieval of waveform data in almost real time, as well as to the staff of KOERI for installing and maintaining the KO network.

Appendix A

Table A1

Earthquakes with $M \geq 6.0$ until 2016 in the broader study area. Parameters for the historical era (until 1900) are from Papazachos and Papazachou (2003), Taxeidis (2003), Kouskouna and Sakkas (2013) and Stucchi et al. (2013). For the instrumental era, I_{max} and description/damage are from Papazachos and Papazachou (2003) and all other parameters from Makropoulos et al. (2012).

Yr	Mo	Dy	Lat(°N)	Lon(°E)	M/ M_e	I_{max} (Locality)	Description/Damage
-496	0	0	38.40	26.20	6.0	VIII (Chios)	Collapse of a school's roof. At least 119 casualties.
-231	0	0	39.20	26.30	6.8	X (Lesvos)	Destruction and partial submersion underwater of the ancient city of Pyrrha.
1383	8	6	39.30	26.40	6.8	IX (Mytilene)	Major damage throughout Lesvos island, with 500 casualties.
1389	3	20	38.70	26.20	6.7	VIII (Chios)	Severe damage throughout the island of Chios. Felt in nearby islands and the coast of Asia Minor, causing significant damage.
1636	2	27	39.20	26.20	6.2	VII (Lesvos)	Several buildings were destroyed.
1674	1	23	38.70	26.30	6.2	VII (Chios)	Minor damage to buildings. Felt in Asia Minor.
1772	11	24	38.60	26.70	6.4	VIII (Foça)	Severe damage in the city of Foça. Building collapses in Lesvos. Felt in Chios.
1778	7	3	38.40	26.80	6.4	IX (İzmir)	Severe damage and major collapses in İzmir due to the mainshock. City walls collapsed due to an equally violent aftershock. Damage was observed in other areas to the west. Over 200 casualties.
1845	10	11	39.10	26.30	6.7	VIII-IX (Lisvori, Lesvos)	Extreme damage to the building stock of the island, with multiple building collapses. In Lisvori, only 2 houses were left standing, out of 70 or 80. Several slope failures led to additional damage to housing. One casualty and 60 houses destroyed in Vrissa
1863	8	16	38.30	26.10	6.2	VIII (Chios)	Extended damage in Chios and adjacent areas.
1865	7	23	39.40	26.30	6.6	IX (Lesvos)	Most of the housing in Molyvos village was destroyed. Several damages to nearby villages, with 100 building collapses.
1867	3	7	39.20	26.25	7.0	X (Kloumidados, Lesvos)	A total of 4746 buildings collapsed and 5529 were damaged in the broader area of Mytilene, with 550 casualties. Out of the 70 villages of the island, only 5 or 6 were not damaged. Considerable damage in Asia Minor.
1883	10	15	38.40	26.60	6.8	IX (Çeşme)	A total of 3600 building collapses and 120 casualties were observed in Çeşme. Building collapses were also observed in İzmir. The earthquake was felt as far as Athens.
1889	10	25	39.20	25.90	6.8	IX (Lesvos)	Extreme damages in 1800 houses and 36 casualties. Strong shaking was felt in nearby areas, up to Istanbul.
1890	5	26	38.50	25.50	6.2	VII (Psara)	One building collapse and slight damage. Felt in Chios.
1919	11	18	39.41	26.09	7.0	IX (W Turkey)	Destruction of villages in epicentral distances up to 50 km. Severe damage in Mytilene and minor in İzmir and Chios.
1939	9	22	38.78	26.73	7.0	VIII (W Turkey)	Severe damage in areas near the epicenter.
1944	10	6	39.46	26.43	7.0	IX (NW Turkey)	Severe damage in areas as far as Lesvos.
1949	7	23	38.71	26.27	7.0	IX (Chios)	In Chios, 534 houses collapsed, 2526 showed major damage and 2985 minor, while 3 casualties were reported. Damage from Psara (to the west) to Foça (to the east).

Table A2

Parameters of focal mechanisms used for the inversion of the tectonic stress. *: Kassaras et al. (2016), **: (<http://www.geophysics.geol.uoa.gr>).

Yr	Mo	Dy	Hr	Mn	Sc	Lat (°N)	Lon (°E)	Depth (km)	Mag	Strike(°)	Dip(°)	Rake(°)	Source
1919	11	18	21	54	57.0	39.4100	26.0900	20.0	7.0	98	45	-97	*
1949	7	23	15	3	35.0	38.7100	26.2700	17.0	7.0	250	46	-127	*
1979	6	14	11	44	45.0	38.7940	26.5730	15.2	5.9	121	42	-50	*
2001	7	18	0	58	21.0	38.7300	25.9700	15.0	4.1	255	36	-132	*
2003	12	16	10	41	10.0	38.9700	26.8300	15.0	4.5	304	45	-51	*
2004	11	22	19	13	34.0	38.6000	25.6000	18.0	5.0	235	51	-171	*
2005	8	24	3	6	20.0	39.6800	25.5600	29.0	4.6	56	74	-171	*
2006	7	12	14	40	55.0	38.8000	26.8000	24.0	4.3	52	75	167	*
2007	1	8	3	35	45.0	39.4800	25.8200	14.0	4.0	224	40	172	*
2007	6	5	7	27	51.8	38.7040	26.0610	8.0	4.0	51	79	-172	*
2007	6	10	8	15	10.0	38.8700	26.3800	17.0	3.9	241	75	169	*
2007	6	12	13	12	59.3	38.9300	26.4500	13.0	4.3	339	51	14	*
2007	9	9	5	14	57.0	38.8400	26.4200	10.0	4.2	335	79	1	*
2007	11	9	1	43	2.8	38.8050	25.6740	16.0	5.0	62	69	-172	*
2007	11	9	7	7	39.0	38.7660	25.7910	15.0	4.3	44	86	177	*
2007	11	9	7	11	57.0	38.7470	25.7660	20.0	4.6	242	71	-177	*
2007	11	9	13	0	44.0	38.8000	25.8000	18.0	3.6	239	71	-162	*
2007	11	10	11	28	30.0	38.8000	25.7000	22.0	3.9	54	67	-168	*
2008	1	12	15	6	45.0	38.8796	26.0159	20.0	4.4	71	59	-164	*
2008	1	15	7	44	25.3	38.8628	25.9885	14.0	3.8	240	64	179	*
2008	7	31	2	54	52.3	38.8738	26.0979	12.0	4.1	344	51	-13	*
2008	7	31	3	4	16.5	38.8702	26.1085	14.0	3.7	1	61	24	*
2009	3	1	0	46	5.2	38.8687	26.0874	14.0	3.8	349	87	3	*
2009	3	30	22	22	39.3	38.9035	26.1098	8.0	3.6	285	38	-120	*
2010	5	11	5	23	37.8	39.4512	25.9312	11.0	3.8	180	30	-110	*
2010	5	11	7	3	37.1	39.4512	25.9312	8.0	3.9	135	45	-115	*
2010	6	6	7	22	31.9	39.0024	26.0825	8.0	3.8	290	30	-80	*
2010	12	11	23	2	19.0	38.4904	25.5915	30.0	4.1	246	53	-155	*
2011	11	13	1	5	0.0	38.4883	25.5923	13.0	3.7	230	77	-177	*
2011	12	5	8	17	27.0	38.8297	26.3338	20.0	4.7	59	66	-165	*
2011	12	5	8	30	25.0	38.8460	26.3210	27.0	4.0	325	57	-27	*
2011	12	5	8	42	56.0	38.8680	26.2800	15.0	3.3	341	82	8	*
2012	4	27	10	49	5.0	38.6500	26.6200	26.0	3.5	239	71	-178	*
2012	5	2	11	37	7.0	38.6500	26.6500	19.0	3.8	230	70	-161	*
2013	1	8	14	16	9.0	39.6580	25.5300	16.0	5.7	331	78	-5	*
2013	1	9	15	41	33.0	39.6790	25.6070	17.0	4.4	149	75	-15	*
2013	1	12	0	30	21.0	39.6650	25.4950	15.0	4.3	68	56	-175	*
2013	1	12	20	50	11.4	38.8320	25.9740	12.0	3.8	235	61	-162	*
2013	1	13	8	55	15.8	39.7090	25.6040	10.0	4.4	336	73	-1	*
2013	1	13	17	54	33.5	39.6390	25.6470	12.0	3.9	328	73	-5	*
2013	2	10	18	10	43.0	39.7190	25.5860	19.0	3.8	152	72	-8	*
2013	4	1	16	54	56.7	38.8250	25.9990	13.0	4.1	236	65	-169	*
2013	4	11	8	39	41.5	39.1810	26.3030	6.0	3.7	44	48	179	*
2013	6	9	15	15	8.0	38.7900	26.9500	16.0	3.9	248	41	-137	*
2014	1	13	10	51	27.7	39.7749	26.0774	12.0	3.9	293	33	-60	*
2015	9	10	8	12	45.0	38.8185	26.2508	15.0	4.7	87	36	-121	*
2017	1	14	22	39	0.3	39.4669	26.1228	9.0	4.4	321	51	-53	**
2017	1	15	4	3	20.8	39.5131	26.0587	19.3	3.9	307	38	-45	**
2017	2	6	3	51	40.7	39.5215	26.1578	13.0	5.2	103	47	-137	**
2017	2	6	10	58	2.6	39.4943	26.0894	11.0	5.1	90	38	-137	**
2017	2	6	11	45	1.2	39.4860	26.0418	11.0	4.2	294	34	-50	**
2017	2	7	2	24	3.7	39.4898	26.1677	12.0	5.2	87	33	-116	**
2017	2	7	5	15	50.7	39.4919	26.1840	11.0	4.1	137	46	-59	**
2017	2	7	5	17	10.1	39.4672	25.8954	12.0	4.2	340	44	-52	**
2017	2	7	21	0	55.1	39.5028	26.1184	11.0	4.1	306	46	-54	**
2017	2	7	21	35	0.1	39.5147	26.1357	11.0	4.0	322	48	-25	**
2017	2	8	1	38	5.9	39.4898	26.1784	12.0	4.5	328	49	-30	**
2017	2	8	2	16	14.9	39.5138	26.1130	12.0	3.9	316	44	-14	**
2017	2	9	10	13	10.7	39.5248	26.0630	10.0	3.9	113	46	-56	**
2017	2	10	8	55	26.2	39.4772	26.1470	11.0	4.5	147	40	-80	**
2017	2	12	13	48	16.1	39.4798	26.1231	12.0	5.1	116	43	-103	**
2017	2	16	0	19	0.5	39.5034	26.0654	13.0	4.5	298	40	-92	**
2017	2	22	1	24	21.9	39.5523	26.0713	11.0	3.6	100	43	-109	**
2017	2	23	1	55	14.7	39.5197	26.0747	9.0	4.2	64	37	-124	**
2017	2	28	23	27	34.7	39.5171	26.1256	11.0	4.6	98	29	-85	**
2017	3	24	15	19	6.2	39.5397	26.0766	12.0	4.0	143	67	25	**

References

- Çağatay, M.N., Gorur, N., Alpar, B., Saatçılar, R., Akkok, R., Sakinc, M., Yuce, H., Yaltirak, C., Kuscü, I., 1998. Geological evolution of the Gulf of Saros, NE Aegean Sea. *Geo Mar. Lett.* 18, 1–9.
- Aktar, M., Karabulut, H., Ozalaybey, S., Childs, D., 2007. A conjugate strike-slip fault system within the extensional tectonics of Western Turkey. *Geophys. J. Int.* 171, 1363–1375.
- Altınok, Y., Alpar, B., Yaltirak, C., Pinar, A., Ozer, N., 2012. The earthquakes and related tsunamis of October 6, 1944 and March 7, 1867; NE Aegean Sea. *Nat. Hazards* 60, 3–25.

- Angelier, J., Tarantola, A., Valette, B., Manoussis, S., 1982. Inversion of field data in fault tectonics to obtain the regional stress I. Single phase fault populations: a new method of computing the stress tensor. *Geophys. J. R. Astron. Soc.* 69, 607–621.
- Angelier, J., 1979. Determination of the mean principal directions of stresses for a given fault population. *Tectonophysics* 56, T17–T26.
- Angelier, J., 1984. Tectonic analysis of fault slip data sets. *J. Geophys. Res.* 89, 5835–5848.
- Antoniou, V., Andreadakis, E., Mavroulis, S., Spyrou, N.I., Skourtsos, E., Lekkas, E., Carydis, P., 2017. Post-earthquake rapid assessment using Unmanned Aircraft Systems (UAS) and GIS online applications: the case of Vrissa settlement after the 2017 June 12, Mw 6.3 Lesvos earthquake (North Aegean Sea, Greece). In: *PATA DAYS 2017: 8th International Workshop on Paleoseismology, Active Tectonics and Archeoseismology*, 13–16 November 2017. Blenheim, New Zealand.
- Armijo, R., Flerit, F., King, G., Meyer, B., 2003. Linear elastic fracture mechanics explains the past and present evolution of the Aegean. *Earth Planet. Sci. Lett.* 217, 85–95.
- Arvidsson, R., Grunththal, G., SHARE Working Group, 2010. Compilation of existing regional and national seismic source zones. Deliverable of the SHARE EC Project.
- Barakou, Th., Delibasis, N., Voulgaris, N., Baier, B., 2001. Seismotectonic features in the northern Aegean Sea. *Bull. Geol. Soc. Greece* 34, 1449–1456.
- Barka, A., Reilinger, R., 1997. Active Tectonics of Eastern Mediterranean region: deduced from GPS, neotectonic and seismicity data. *Annali Di Geofisica X2* (3), 587–610.
- Bott, M.H.P., 1959. The mechanics of oblique slip faulting. *Geol. Mag.* 96, 109–117.
- Bouchon, M., 1981. A simple method to calculate Green's functions for elastic layered media. *Bull. Seismol. Soc. Am.* 71 (4), 959–971.
- Chatelain, J., 1978. Étude fine de la sismicité en zone de collision continentale à l'aide d'un réseau de stations portables: la région Hindu-Kush-Pamir. Ph.D. thesis. Université Paul Sabatier, Toulouse.
- Chatzipetros, A., Kiratzi, A., Sboras, S., Zouros, N., Pavlides, S., 2013. Active faulting in the north-eastern Aegean Sea Islands. *Tectonophysics* 597–598, 106–122.
- Chiarabba, C., Frepoli, A., 1997. Minimum 1D velocity models in Central and Southern Italy: a contribution to better constrain hypocentral determinations. *Ann. Geophys.* 40 (4), 937–954.
- Delibasis, N.D., Voulgaris, N.S., 1989. Microseismic and seismotectonic study of the island of Lesbos. In: *Proc. 4th Inter. Semin. Results EC Geothermal Energy Res. and Demon. Florence*, 27–30 April 1989, pp. 474–481.
- EL-STAT, 2011. Hellenic Statistical Authority – 2011 General Censuses of Buildings and Population-Housing.
- Earthquake Planning and Protection Organization (EPPO), 2014. Protection Measures – Post-Seismic Period, Athens (in Greek).
- Eberhart-Phillips, D., 1986. Three-dimensional velocity structure in northern California Coast Ranges from inversion of local earthquake arrival times. *Bull. Seismol. Soc. Am.* 76, 1025–1052.
- Ekström, G., England, P., 1989. Seismic strain rates in regions of distributed continental deformation. *J. Geophys. Res.* 94, 10231–10257.
- Ekström, G., Nettles, M., Dziewonski, A.M., 2012. The global CMT project 2004–2010: centroid-moment tensors for 13,017 earthquakes. *Phys. Earth Planet. Inter.* 200–201, 1–9.
- Ferentinis, G., Brooks, M., Collins, M.B., 1981. Gravity-induced deformation on the northern flank and floor of the Sporades Basin of the North Aegean Sea trough. *Mar. Geol.* 44 (289), 302.
- Ganas, A., Drakatos, G., Pavlides, S.B., Stavrakakis, G.N., Ziazia, M., Sokos, E., Karastathis, V.K., 2001. The 2001 Mw = 6.4 Skyro earthquake, conjugate strike-slip faulting and spatial variation in stress within the central Aegean Sea. *J. Geodyn.* 39 (1), 61–77.
- Ganas, A., Oikonomou, A., Tsimi, C., 2013. NOFAULTS: a digital database for active faults in Greece. *Bull. Geol. Soc. Greece XLVII* (2), 518–530.
- Gephart, J.W., Forsyth, D.W., 1984. An improved method for determining the regional stress tensor using earthquake focal mechanism data: application to the San Fernando earthquake sequence. *J. Geophys. Res.* 89, 9305–9320.
- Golub, G.H., Van Loan, C.F., 1996. *Matrix Computations*. The Johns Hopkins University Press, New York pp. 448.
- Grünthal, G., Musson, R.M.W., Schwarz, J., Stucchi, M., 1998. *European Macroseismic Scale 1998 (EMS-98) Vol. 5 Centre Européen de Géodynamique et de Séismologie*, Luxembourg.
- Gutenberg, B., Richter, C.F., 1944. Frequency of earthquakes in California. *Bull. Seism. Soc. Am.* 4, 185–188.
- Hardebeck, J.L., Hauksson, E., 2001. Stress orientations obtained from earthquake focal mechanisms: what are appropriate uncertainty estimates. *Bull. Seismol. Soc. Am.* 91 (2), 250–262.
- Hardebeck, J.L., Michael, A.J., 2006. Damped regional-scale stress inversions: methodology and examples for southern California and the Coalinga aftershock sequence. *J. Geophys. Res.* 111, B11310.
- Hecht, J., 1972. Geological Map of Greece, Plomari-Mytilini Sheet. I.G.M.E., Greece scale 1:50,000.
- Hecht, J., 1974a. Geological Map of Greece, Eressos Sheet. I.G.M.E., Greece scale 1:50,000.
- Hecht, J., 1974b. Geological Map of Greece, Polychnitos Sheet. I.G.M.E., Greece scale 1:50,000.
- KOERI, 2001. International Federation of Digital Seismograph Networks. Other/Seismic Network. 10.7914/SN/KO. Bogazici University Kandilli Observatory And Earthquake Research Institute.
- Kahle, H.G., Straub, C., Reilinger, R., McClusky, S., King, R., Hurst, K., Veis, G., Kastens, K., Cross, P., 1998. The strain rate field in the eastern Mediterranean region estimated by repeated GPS measurements. *Tectonophysics* 294, 237–252.
- Kapetanidis, V., Deschamps, A., Papadimitriou, P., Matrullo, E., Karakonstantis, A., Bozionelos, G., Kaviris, G., Serpetsidaki, A., Lyon-Caen, H., Voulgaris, N., Bernard, P., Sokos, E., Makropoulos, K., 2015. The 2013 earthquake swarm in Helike, Greece: seismic activity at the root of old normal faults. *Geophys. J. Int.* 202, 2044–2073.
- Kapetanidis, V., 2017. Spatiotemporal patterns of microseismicity for the identification of active fault structures using seismic waveform cross-correlation and double-difference relocation. PhD Thesis. Department of Geophysics-Geothermics, Faculty of Geology and Geoenvironment, University of Athens, Greece.
- Karakonstantis, A., 2017. 3-D Simulation of Crust and Upper Mantle Structure in the Broader Hellenic Area Through Seismic Tomography. Ph.D. Thesis. Department of Geophysics-Geothermics, Faculty of Geology, University of Athens, Greece in Greek.
- Kassaras, I., Kapetanidis, V., 2017. A TUTORIAL: Resolving the tectonic stress by the inversion of earthquake focal mechanisms. Application in the region of Greece. In: *D'Amico, S. (Ed.), Moment Tensor Solutions – A Useful Tool for Seismotectonics*. Springer-Verlag.
- Kassaras, I., Kapetanidis, V., Karakonstantis, A., Kaviris, G., Papadimitriou, P., Voulgaris, N., Makropoulos, K., Popandopoulos, G., Moshou, A., 2014a. The April-June 2007 Trichonis Lake earthquake swarm (W. Greece). New implications toward the causative fault zone. *J. Geodyn.* 73, 60–80.
- Kassaras, I., Kapetanidis, V., Karakonstantis, A., Kouskouna, V., Ganas, A., Chouliaras, G., Drakatos, G., Moshou, A., Mitropoulou, V., Argyrakas, P., Lekkas, E., Makropoulos, K., 2014b. Constraints on the dynamics and spatio-temporal evolution of the 2011 Oichalia seismic swarm (SW Peloponnese, Greece). *Tectonophysics* 614, 100–127.
- Kassaras, I., Kapetanidis, V., Karakonstantis, A., 2016. On the spatial distribution of seismicity and the 3D tectonic stress field in western Greece. *Phys. Chem. Earth* 95, 50–72.
- Katsikatsos, G., Mataragas, D., Migiros, G., Triandafillou, E., 1982. Geological Study of Lesbos Island. Special Report. I.G.M.E., Greece.
- Katsikatsos, G., Migiros, G., Triantaphyllis, M., Mettos, A., 1986. Geological Structure of the Internal Hellenides (E. Thessaly- SW. Macedonia, Euboea-Attica-Northern Cyclades Islands and Lesvos). I.G.M.E. Geological and Geophysical Research, pp. 191–212 Sp. Issue.
- Kaviris, G., 2003. Study of Seismic Source Properties of the Eastern Gulf of Corinth. Ph.D. Thesis. Department of Geophysics-Geothermics, Faculty of Geology, University of Athens, Greece in Greek.
- King, G.C.P., Stein, R.S., Lin, J., 1994. Static stress changes and the triggering of earthquakes. *Bull. Seismol. Soc. Am.* 84 (3), 935–953.
- Kiratzi, A., Louvari, E., 2003. Focal mechanisms of shallow earthquakes in the Aegean Sea and the surrounding lands determined by waveform modelling: a new database. *J. Geodyn.* 36, 251–274.
- Kiratzi, A., Wagner, G., Langston, C., 1991. Source parameters of some large earthquakes in Northern Aegean determined by body waveform inversion. *Pure Appl. Geophys.* 105, 515–527.
- Kiratzi, A., 2002. Stress tensor inversions along the westernmost North Anatolian Fault Zone and its continuation into the North Aegean Sea. *Geophys. J. Int.* 151, 360–376.
- Kiratzi, A., 2014. Mechanisms of Earthquakes in Aegean. *Encyclopedia of Earthquake Engineering*. Springer-Verlag, Berlin, Heidelberg. http://dx.doi.org/10.1007/978-3-642-36197-5_299-1.
- Kissling, E., Ellsworth, W.L., Eberhart-Phillips, D., Kradolfer, U., 1994. Initial reference models in local earthquake tomography. *J. Geophys. Res.* 99 (10), 19635–19646.
- Klein, F.W., 1989. User's guide to HYPOINVERSE, a program for VAX computers to solve earthquake locations and magnitudes. U.S. Geological Survey Open-File Report 89-314, pp. 1–58.
- Kouskouna, V., Sakkas, G., 2013. The University of Athens Hellenic Macroseismic Database (HMDB.UoA): historical earthquakes. *J. Seismol.* 17 (4), 1253–1280.
- Kreemer, C., Holt, W.E., Haines, A.J., 2003. An integrated global model of present-day plate motions and plate boundary deformation. *Geophys. J. Int.* 154 (1), 8–34.
- Kreemer, C., Blewitt, G., Klein, E.C., 2014. A geodetic plate motion and global strain rate model. *Geochem. Geophys. Geosyst.* 15, 3849–3889.
- Lekkas, E., Voulgaris, N., Karydis, P., Tselentis, G.A., Skourtsos, E., Antoniou, V., Andreadakis, E., Mavroulis, S., Spirou, N., Speis, F., Papadimitriou, P., Kouskouna, V., Kassaras, I., Kaviris, G., Pavlou, K., Sakkas, V., Chouliaras, G., 2017a. Preliminary Report on the 12 June, 2017: Lesvos (Greece) Earthquake. *Paleoseismicity.org* <http://paleoseismicity.org/preliminary-report-on-the-12-june-2017-lesvos-greece-earthquake/#more-8735>.
- Lekkas, E., Carydis, P., Skourtsos, E., Mavroulis, S., Andreadakis, E., Antoniou, V., Spyrou, N.I., 2017b. Factors controlling the distribution of building damage in the traditional Vrissa settlement induced by the 2017 June 12, Mw 6.3 Lesvos earthquake (Northeastern Aegean Sea, Greece). In: *PATA DAYS 2017: 8th International Workshop on Paleoseismology, Active Tectonics and Archeoseismology*, 13–16 November 2017. Blenheim, New Zealand.
- Lekkas, E., Voulgaris, N., Karydis, P., Tselentis, G.A., Skourtsos, E., Antoniou, V., Andreadakis, E., Mavroulis, S., Spirou, N.I., Speis, F., Papadimitriou, P., Kouskouna, V., Kassaras, I., Kaviris, G., Pavlou, K., Sakkas, V., Chouliaras, G., 2017c. Lesvos Earthquake Mw 6.3, June 12, 2017. Preliminary Report, Athens.
- Leptokaropoulos, K., Papadimitriou, E., Orlecka-Sikora, B., Karakostas, V., 2014. Forecasting seismicity rates in western Turkey as inferred from earthquake catalog and stressing history. *Nat. Hazards* 73 (3), 1817–1842.
- Lopes, A.E.V., Assumpção, M., 2011. Genetic algorithm inversion of the average 1D crustal structure using local and regional earthquakes. *Comput. Geosci.* 37 (9), 1372–1380.
- Makropoulos, K.C., Burton, P.W., 1981. A catalogue of seismicity in Greece and the adjacent areas. *Geophys. J. R. Astr. Soc.* 65, 741–762 and Microfiche GJ65/1.
- Makropoulos, K., Kaviris, G., Kouskouna, V., 2012. An updated and extended earthquake catalogue for Greece and adjacent areas since 1900. *Nat. Hazards Earth Syst. Sci.* 12, 1425–1430.
- Maley, T.S., Johnson, L.G., 1971. Morphology and structure of the Aegean Sea. *Deep-Sea Res.* 18, 109–122.

- Martínez-Garzón, P., Kwiatek, G., Ickrath, M., Bohnhoff, M., 2014. MSATSI: a MATLAB package for stress inversion combining solid classic methodology anew simplified user-handling and a visualization tool. *Seismol. Res. Lett.* 85 (4), 896–904.
- Mascle, J., Martin, L., 1990. Shallow structure and recent evolution of the Aegean Sea: a synthesis based on continuous reflection profiles. *Mar. Geol.* 94, 271–299.
- Michael, A.J., 1984. Determination of stress from slip data: faults and folds. *J. Geophys. Res.* 89, 11517–11526.
- Michael, A.J., 1987. Use of focal mechanisms to determine stress: a control study. *J. Geophys. Res.* 92, 357–368.
- Michael, A.J., 1991. Spatial variations in stress within the 1987 Whittier Narrows California aftershock sequence: new techniques and results. *J. Geophys. Res.* 96, 6303–6319.
- Mignan, A., Chouliaras, G., 2014. 50 years of seismic network performance in Greece (1964–2013): spatiotemporal evolution of the completeness magnitude. *Seismol. Res. Lett.* 85 (3), 657–667.
- Nalbant, S.S., Hubert-Ferrari, A., King, G.C.P., 1998. Stress coupling between earthquakes in northwestern Turkey and the north Aegean sea. *J. Geophys. Res.* 103, 24469–24486.
- Nash, J.C., 1990. The singular-value decomposition and its use to solve least-squares problems. *Compact Numerical Methods for Computers: Linear Algebra and Function Minimisation*, 2nd ed. Adam Hilger, Bristol, England, pp. 30–48 Ch. 3.
- Otsubo, M., Yamaji, A., 2006. Improved resolution of the multiple inverse method by eliminating erroneous solutions. *Comput. Geosci.* 32, 1221–1227.
- Otsubo, M., Yamaji, A., Kubo, A., 2008. Determination of stresses from heterogeneous focal mechanism data: an adaptation of the multiple inverse method. *Tectonophysics* 457, 150–160.
- Papadimitriou, P., Kaviris, G., Karakonstantis, A., Makropoulos, K., 2010. The Cornet seismological network: 10 years of operation, recorded seismicity and significant applications. *AGPH* 45, 193–208.
- Papadimitriou, P., Chousianitis, K., Agalos, A., Moshou, A., Lagios, E., Makropoulos, K., 2012. The spatially extended 2006 April Zakynthos (Ionian Islands, Greece) seismic sequence and evidence for stress transfer. *Geophys. J. Int.* 190 (2), 1025–1040.
- Papadimitriou, P., Kapetanidis, V., Karakonstantis, A., Kaviris, G., Voulgaris, N., Makropoulos, K., 2015. The Santorini volcanic complex: a detailed multi-parameter seismological approach with emphasis on the 2011–2012 unrest period. *J. Geodyn.* 85, 32–57.
- Papazachos, B.C., Papazachou, C., 2003. The Earthquakes of Greece. Ziti Publ. Co., Thessaloniki, Greece p. 286 (in Greek).
- Papazachos, B.C., Kiratzi, A.A., Hatzidimitriou, P., Rocca, A., 1984. Seismic faults in the Aegean area. *Tectonophysics* 106, 71–85.
- Pe-Piper, G., Piper, D.J.W., 1993. Revised stratigraphy of the Miocene volcanic rocks of Lesbos, Greece. *Neues Jahrbuch Geologie und Palaeontologie Munchen* 2, 97–110.
- Pe-Piper, G., 1978. Cainozoic Volcanic Rocks of Lesbos Island. Ph.D. Thesis. University of Patras 365 p.
- Reilinger, R., McClusky, S.C., Oral, M.B., King, R.W., Toksoz, M.N., Barka, A.A., Kinik, I., Lenk, O., Sanli, I., 1997. Global positioning system measurements of present-day crustal movements in the Arabia-Africa-Eurasia plate collision zone. *J. Geophys. Res.* 102, 9983–9999.
- Roussos, N., Lyssimachou, T.R., 1991. Structure of the Central North Aegean Trough: an active strike-slip deformation zone. *Basin Res.* 3, 39–48.
- Saatçilar, R., Ergintav, S., Demirbag, E., Inan, S., 1999. Character of active in the North Aegean Sea. *Mar. Geol.* 160, 339–353.
- Saner, S., 1985. Sedimentary sequences and tectonic setting of Saros Gulf area NE Aegean Sea, Turkey. *Bull. Geol. Soc. Turkey* 28, 1–10.
- Shcherbakov, R., Turcotte, D.L., 2004. A modified form of Bath's law. *Bull. Seismol. Soc. Am.* 94, 1968–1975.
- Soulakellis, N., Novak, I., Zouros, N., Lowman, P., Yates, J., 2006. Fusing landsat-5/TM imagery and shaded relief maps in tectonic and geomorphic mapping: Lesbos Island photogrammetric Greece. *Eng. Remote Sens.* 72 (6), 693–700.
- Stein, R.S., 1999. The role of stress transfer in earthquake occurrence. *Nature* 402, 605–609.
- Stucchi, M., Rovida, A., Gomez Capera, A.A., Alexandre, P., Camelbeeck, T., Demircioglu, M.B., Gasperini, P., Kouskoua, V., Musson, R.M.W., Radulian, M., Sesetyan, K., Vilanova, S., Baumont, D., Bungum, H., Fäh, D., Lenhardt, W., Makropoulos, K., Martinez Solares, J.M., Scotti, O., Zivcic, M., Albini, P., Battlo, J., Papaioannou, C., Tatevossian, R., Locati, M., Meletti, C., Viganò, D., Giardini, D., 2013. The SHARE European Earthquake Catalog (SHEEC) 1000–1899. *J. Seismol.* 17 (2), 523–544.
- Taxeidis, K., 2003. Study of Historical Seismicity of the Eastern Aegean Islands. Ph.D. Thesis. Department of Geophysics-Geothermics, Faculty of Geology, University of Athens, Greece 301 pp (in Greek).
- Taymaz, T., Jackson, J.A., McKenzie, D., 1991. Active tectonics of the North and Central Aegean Sea. *Geophys. J. Int.* 106, 433–490.
- Taymaz, T., Yilmaz, Y., Dilek, Y., 2007. The geodynamics of the Aegean and Anatolia: introduction. *Geol. Soc. Lond. Spec. Publ.* 291, 1–16.
- Toda, S., Stein, R.S., Sevilgen, V., Lin, J., 2011. *Coulomb 3.3 Graphic-rich deformation and stress-change software for earthquake, tectonic, and volcano research and teaching-user guide*. U.S. Geological Survey Open-File Report 2011-1060. pp. 63. <http://pubs.usgs.gov/of/2011/1060/>.
- Voulgaris, N., Parcharidis, I., Pahoula, M., Pirlis, E., 2004. Correlation of tectonics, seismicity and geothermics of Lesbos Island using remote sensing data and geographical information systems. *Bull. Geol. Soc. Greece XXXVI*, 938–947.
- Waldhauser, F., 2001. HypoDD-A Program to Compute Double-Difference Hypocenter Locations. U.S. Geol. Surv. Open File Rep.01-113. 25 p.
- Wallace, R.E., 1951. Geometry of shearing stress and relation to faulting. *J. Geol.* 59, 118–130.
- Woessner, J., Laurentiu, D., Giardini, D., Crowley, H., Cotton, F., Grünthal, G., Valensise, G., Arvidsson, R., Basili, R., Demircioglu, M.B., Hiemer, S., Meletti, C., Musson, R.W., Rovida, A.N., Sesetyan, K., Stucchi, M., 2015. The 2013 European seismic hazard model: key components and results. *Bull. Earthquake Eng.* 13, 3553–3596.
- Yaltirak, C., Alpar, B., 2002. Evolution of the NAF Middle segment and shallow seismic investigation of the Southeastern Sea of Marmara (Gemlik Bay). *Mar. Geol.* 190, 307–327.
- Yaltirak, C., Alpar, B., Sakinc, M., Yuce, H., 2000. Origin of the strait of Canakkale (Dardanelles): regional tectonics and the mediterranean-Marmara incursion. *Mar. Geol.* 164, 139–156.
- Yaltirak, C., Isiller, E.B., Aksu, A.E., Hiscott, R.N., 2012. Evolution of the Bababurnu Basin and shelf of the Biga Peninsula: Western extension of the middle strand of the North Anatolian Fault Zone Northeast Aegean Sea, Turkey. *J. Asian Earth Sciences* 57, 103–119.
- Yamaji, A., Sato, K., 2011. A spherical code and stress tensor inversion. *Comput. Geosci.* 38 (1), 164–167.
- Yamaji, A., Otsubo, M., Sato, K., 2006. Paleostress analysis using the Hough transform for separating stresses from heterogeneous fault-slip data. *J. Struct. Geol.* 28, 980–990.
- Yamaji, A., 2000. The multiple inverse method: a new technique to separate stresses from heterogeneous fault-slip data. *J. Struct. Geol.* 22, 441–452.
- Yolsal-Çevikbilen, S., Taymaz, T., Helvacı, C., 2014. Earthquake mechanisms in the Gulfs of Gökova, Sığacık, Kusadası, and the Simav Region (western Turkey): neotectonics, seismotectonics and geodynamic implications. *Tectonophysics* 635, 100–124.
- Zouros, N., Pavlides, S., Soulakellis, N., Chatzipetros, A., Vasileiadou, K., Valiakos, I., Mpentana, K., 2011. Using active fault studies for raising public awareness and sensitisation on seismic hazard: a case study from Lesbos Petrified Forest Geopark NE Aegean Sea, Greece. *Geoheritage* 3, 317–327.